Synthesis, Characterisation, and Catalytic Evaluation of Ru-ONO Complexes featuring N- and P-based ligands

Babatunde Awe,[a] Glendin Swart,[b] Elizabeth Erasmus,[b] Frederick P. Malan*[a]

[a] *Department of Chemistry, University of Pretoria, Lynnwood Road, Hatfield, Pretoria, 0002, South Africa.*

[b] *Department of Chemistry, University of the Free State, Nelson Mandela Drive, Bloemfontein, 9300, South Africa.*

*Corresponding author: Dr Frikkie Malan (frikkie.malan@up.ac.za)

Graphical Abstract

Nine ruthenium complexes with nitrogen and phosphorus donor ligands derived from a rigid ONO-pincer ligand are synthesised and fully characterised. These complexes show moderate catalytic activity in hydrogenation reactions with up to 96 % conversion in transfer hydrogenation of alcohols within 1 hour. Electrochemical and DFT studies reveal further insights into their electronic and structural properties.

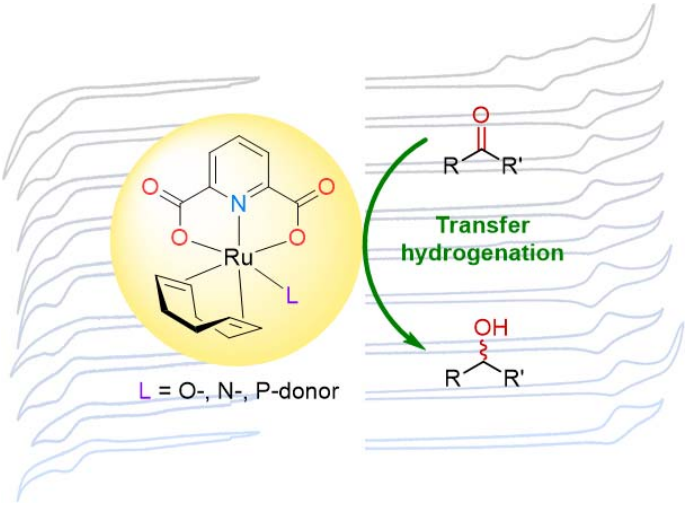

Abstract

Nine new ruthenium complexes featuring nitrogen and phosphorus donor ligands were synthesised from a Ru precursor featuring a rigid ONO-pincer ligand. The choice of nitrogen- and phosphorous-based ancillary ligands was guided by a careful evaluation of their different electronic and steric properties. This evaluation aimed to understand how these ligands, once coordinated, could influence the structural, electronic, and catalytic activity of the corresponding complexes. The range of

complexes showed moderate catalytic activity in the transfer hydrogenation of alcohols, with the best performing catalyst achieving 96% conversion in 1 hour (TON = 96, TOF = 96 h^{-1}). All complexes were characterised using ^{1}H, ^{13}C, ^{31}P (where applicable) NMR spectroscopy, CHN (microanalysis) and HR-MS analyses. Single crystal structures were obtained for all the nine new complexes, as well two new polymorphs of the precursor complex. Complimentary electrochemical (cyclic voltammetry) and density functional theory (DFT) studies provided additional insights into the structural and electronic properties of the different complexes.

Keywords: ruthenium, ONO-pincer ligands, crystallography, transfer hydrogenation.

Introduction

Dipicolinic acid-based ligands (pdc) featuring nitrogen and oxygen atoms that are all potential donors, have been found to coordinate with a range of different (transition) metals including V,[1] Cr, Fe, Mn, Co, Ni, Zn,[2–4] Zr[5], Ca,[5] Cu,[6] Ga,[7] Y,[8] Mo,[9] Ru,[10] Sn,[11] Pt,[12] Pd,[13] and Hg.[14] Complexes of lanthanides and actinides (Eu[15], Gd[15],La,[16] Ce,[17] U,[18,19]) containing coordinated pdc ligands are also known. In coordination chemistry, variable coordination modes refer to the ability of a ligand to bind to a central metal atom or ion in different ways, utilising multiple donor atoms or bonding orientations. This versatility often results in diverse structural geometries and influences the chemical reactivity and stability of the metal complex.[20-21] The combination of the variable coordination modes, a range of biologically active properties,[11,14,16-18] as well as the chemically tunable potential of pdc is seen as the primary driver behind the development of complexes featuring this ligand and its derivatives.[15,22] The pdc ligand may act as a neutral, mono-basic, or dibasic ligand donor (more than twelve possible coordination modes), although the dibasic tridentate mode is most frequently encountered (Figure 1).[20]

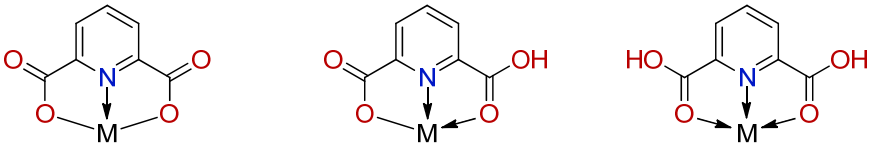

Figure 1. Variable protonated forms of pdc as a tridentate ONO pincer ligand.

Interaction with metals takes place in a pincer-type manner whereby they typically form stable meridional five-membered metallacycles. These metallacycles describe cyclic structures where three

donor atoms from a tridentate ligand form a five-membered ring with a central metal atom, arranged in a meridional (*mer*) configuration. This geometry stabilises the complex by maximising chelation and minimising ring strain, often enhancing catalytic activity and selectivity in metal-mediated reactions.[21-22] Metal complexes featuring a pdc ligand belongs to a class of pincer complexes (complexes featuring at least one tridentate ligand that binds in a rigid, claw-like fashion), with corresponding imparted chemical, structural, and electronic properties. They typically exhibit high thermostability and are bench stable.[21–26] Metal complexes featuring pdc-based ligands also found great use as catalysts in a variety of different and important chemical transformations, which include dehydrogenation[27–30], deoxydehydration[31], and olefin oligomerisation[32] reactions. Complexes of ruthenium in particular are well-known for their catalytic and biological activity in diverse applications, making the combination of pdc with ruthenium ideal for the development of multi-functional complexes.[33–36] Despite this, the chemistry and applications of Ru-pdc complexes remains underdeveloped with the only catalytic reactions investigated to date being oxidation reactions of water[37–44], alcohols[45–47] , and alkanes[48]. The known precursor complex, ($HNEt_3$)[RuCl(COD)(dpc)], reported by Qian-Feng Zhang and co-workers has demonstrated potential as a precursor for forming various nitrogen-based adducts through ligand substitution.[48] However, none of these complexes have been evaluated for their catalytic activity. This study therefore aims to develop a series of catalytically active [Ru(cod)(dpc)] complexes stabilised by a range of pnictogen ligands (featuring group 15 donor atoms). The synthesis, characterisation and catalytic evaluation of nine new Ru-dpc complexes featuring nitrogen and phosphorous-based ligands are reported. Complimentary electrochemical (cyclic voltammetry, CV) and theoretical modelling (density functional theory, DFT) studies are included to assess the electrochemical properties and associated (catalytic) potential of the complexes.

Results and Discussion

Synthesis of nitrogen and phosphine Ru-ONO complexes

The known precursor, [Ru(COD)(dpc)(OH_2)] (**C1**), was synthesised using an already established method with appropriate modification.[48] The pdc precursor, 2,6-pyridinedicarboxylic acid, is deprotonated prior to coordination as a critical step in the synthesis of **C1**. As the base, KOH was used instead of the milder triethylamine, as it facilitated a faster reaction and simpler work-up after the reaction. Deprotonation of the pdc precursor was complete after 15 minutes, whereas NEt_3 required excess amounts and at least 30 minutes for comparable conversion. Product purity was also lower when NEt_3 was used, as it is a competing ligand, with ethyl-based aliphatic signals observed in the initial ^{1}H NMR spectra. The nitrogen and the phosphine donor ligands employed are known compounds and include

pyrazole, imidazole, diphenylphosphinoferrocene (dppf) and methyl diphenylphosphinite. Each of the pnictogen ligands was reacted with **C1** in methanol under reflux conditions and an argon atmosphere. The aqua ligand in each case was replaced by either the N- or P-donating ancillary ligand, leading to the synthesis of nine new Ru-ONO complexes (**C2**-**C10**), see Figure 2. The new complexes **C2**-**C10** were characterised using ^{1}H, ^{13}C and ^{31}P NMR (**C9**, **C10** only) spectroscopy, high resolution mass spectroscopy (HR-MS ESI), single crystal XRD, as well as elemental analysis (%CHN). Complexes **C9** and **C10** were purified using column chromatography (acetone as eluent for **C9**) and (DCM/acetone 1:1 as eluent for **C10**), while washing with EtOAc proved sufficient for complexes **C2-C8**. In general, the reaction proceeded smoothly to give the corresponding complexes as yellow to orange microcrystalline solids in a range of yields (37-99%). Spectroscopic evidence for their formation was provided by ^{1}H NMR spectra where characteristic signals of the ancillary ligands were observed. Examples include δ_H 6.32-6.30 and 7.53-7.52 (CH of pyrazole, **C2**), 7.01 and 7.48 (CH of imidazole, **C3**), 6.60 and 6.93 (CH of imidazole, **C5**), and 7.26-7.22 (C_6H_5 of Ph, **C6**). The ^{13}C NMR signals for the respective functional groups appear within the anticipated ranges, consistent with those of closely related compounds. The ^{1}H NMR spectra of **C2**-**C10** revealed variation in the signal positions of the protons of the dipicolinic pincer backbone for example, signals are in the range of δ_H 8.07, and 7.95-7.90 for **C2** while for **C9** they are in the range of δ_H 7.79-7.70. The ^{1}H NMR signals of complexes **C2**-**C10** differed from those in **C1** only by the appearance of the associated signals for the newly coordinated ligands, while signals for the cyclooctadiene (COD) and the pdc ligands remained unaffected. The aliphatic CH_2 proton signals largely remained unaffected post-coordination in **C2**-**C10**, with only minor shifts observed in selected cases. As an extension of the investigation into the type of pnictogen donor ligands, two phosphorous-based ligands (**L9** and **L10**) were also selected.

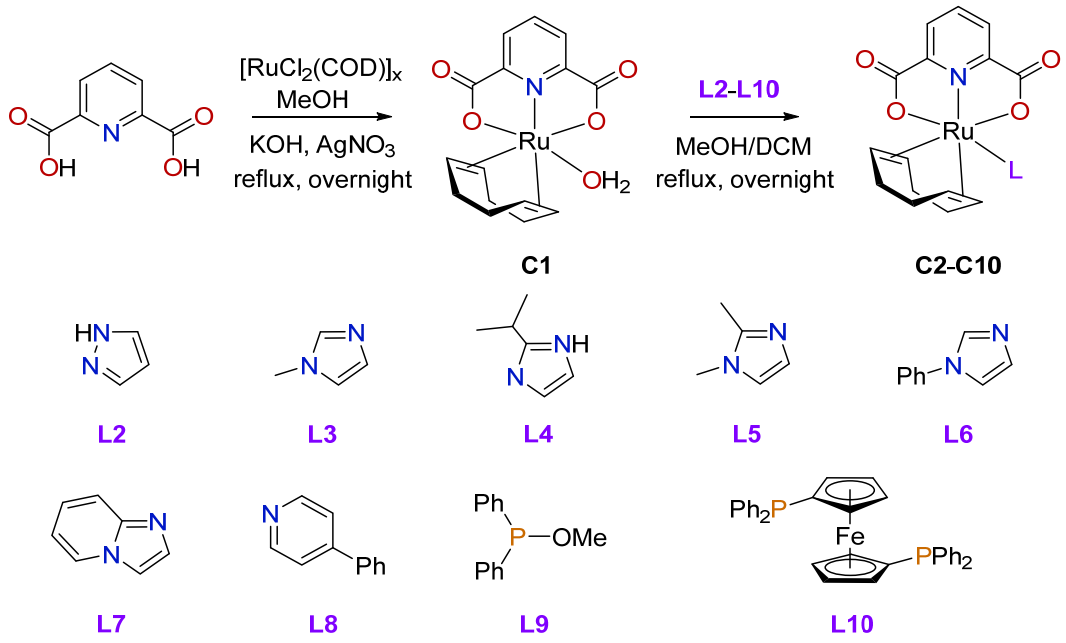

Figure 2. Synthesis of Ru-ONO complexes **C1**-**C10**.

The reactions involving methyl diphenylphosphinite ($PPh_2(OMe)$) and diphenylphosphinoferrocene (dppf) required the use of molecular sieves to afford the corresponding complexes in appreciable yield. The molecular sieves appeared to drive the ligand substitution reaction by inhibiting phosphine oxidation and promoting the uptake of residual water in the reaction mixture. Phosphine coordination in **C9** and **C10** was confirmed using ^{31}P NMR spectroscopy. The chemical shift for phosphorous in **C9** appeared at 125.6 ppm (free ligand at 116.9 ppm), while in **C10** two distinct signals appeared at 27.62 and -19.05 ppm (free ligand shows one resonance at -17.33 ppm). This indicated two unique phosphorous nuclei, where only one P-donor is coordinated to the ruthenium center. This is interesting as the substitution of the relatively labile COD ligand was anticipated to form the complex [Ru(ONO)(dppf)(OH_2)], which was not observed in this case.

X-ray crystallography

Yellow to orange-coloured single crystals of all complexes **C1**-**C10** were obtained from saturated solutions of the complexes in either DCM, acetone, chloroform, or dichloroethane. The crystallographic information for all the complexes is tabulated in the SI (Tables S1-S3), with the molecular structure of **C1-C10** shown in Figures 3-5. Complexes **C1b** and **C3** crystallised in the triclinic crystal system (space group *P*-1), whereas all of the remaining structures in this series (**C2, C4 – C10**) possess monoclinic crystal systems ($P2_1/c$ space group (**C5**, **C6**, **C8**-**C10**), $P2_1/n$ (**C2** and **C7**), $C2/c$ (**C1c**),

I_2/a (**C4**)). The structures of each of the complexes exhibit a Ru(II) centre in a *pseudo*-octahedral geometry with the pdc ligand coordinated at three sites (ONO), two η^2-alkene moieties coordinated in a *cis* fashion (1,5-COD), and a neutral L-donor ligand occupying the sixth coordination site (L = aqua, pyrazole, imidazole derivatives, phosphine derivatives). Octahedral distortion is brought about by the planar, rigid pdc ligand with an average O1-Ru1-O3 bite angle of 153.606(7)° (as opposed to an ideal 180°). Closer to ideal octahedral bond angles are observed with C_{alkene}-Ru1-N1 and C_{alkene}-Ru1-L angles within the ranges of 90.31(5)-95.87(7)° and 86.00(6)-93.64(6)°, respectively. Complex **C1**, being the precursor to complexes **C2**-**C10**, is a known compound with a published crystal structure.[48] In the published structure by Zhang and co-workers[48], **C1a** crystallised in a monoclinic crystal system with space group $P2_1/n$, and unit cell parameters of a = 6.5452(4) Å, b = 12.1810(7) Å, c = 17.4837(10) Å, and β = 94.4010(10)°. In this study, however, two polymorphs[49] of this structure were crystallised and accordingly analysed. The two polymorphic structures of **C1** crystallised in the triclinic *P*-1 (**C1b**) and monoclinic *C*2/*c* (**C1c**) crystal systems. The associated unit cell parameters for the latter two structures are **C1b**: a = 6.5303(5) Å, b = 7.0283(6) Å, c = 16.2104(11) Å, α = 90.128(6)°, β = 99.266(6)°, and γ = 106.746(7)°; **C1c**: a = 18.7224(4) Å, b = 10.4260(2) Å, c = 14.4176(3) Å, β = 92.908(2)°. Interestingly, the unit cell volume of the three structures differs noticeably: 1374.85(4) $Å^3$ (**C1a**), 702.23(6) $Å^3$ (**C1b**), and 2810.69(4) $Å^3$ (**C1c**). None of the three structures contain any solvents of crystallisation. In terms of structural features of the Ru(II) complex molecule in all three structures, the bond lengths and angles agreed to a reasonable extent. The three-dimensional packing of each of the polymorphs differs distinctly in the layers of molecules that stack differently between **C1a**, **C1b**, and **C1c** (see Figure S30, SI).

No noticeable changes in the Ru-C_{alkene}(ave), Ru1-N1, or Ru1-O1/O3 bond lengths, nor in the geometry of the [Ru(pdc)(COD)] fragments were observed upon substitution of the aqua ligand. Substitution of the aqua ligand with pyrazole brings about a Ru1-N2 bond length of 2.1074(14) Å in **C2.** There seems to be a progressive increase in the bond length Ru1-N2 of the complexes due to the influence of the substituent attached to the non-coordinating nitrogen atom and other functional groups present in the coordinated heterocycle (*vide infra*). This is surprising, since it was expected that a stronger electron-donating heterocycle would result in a shorter Ru1-N2 bond. Comparing **C2** (pyrazole), **C3** (*N*-methyl imidazole), **C4** (*N*-isopropyl imidazole) and **C5** (*N*-methyl-2-imidazole), a steady increase in the electron-donating character is anticipated for the N-donor ligand according to the series **C2** < **C3** < **C5** < **C4**. This correlates with corresponding Ru1-N2 bond lengths (Å) in the series 2.1074(14) (**C2**) < 2.114(2) (**C3**) < 2.1570(14) (**C5**) < 2.1823(12) (**C4**). The N-Ph substituent in **C6** is much less electron-donating and hence has an associated Ru1-N2 bond length of 2.104(3) Å. The fused imidazo-pyridine

ligand **L7** in **C7**, and 4'-phenyl-pyridine ligand **L8** in **C8** have similar electron donating properties and lie in the centre of the overall series with Ru1-N2 bond distances of 2.1577(14) Å and 2.1363(15) Å, respectively. All the abovementioned Ru1-N2 bond lengths correspond well with those of similar complexes reported by Zhang and co-workers[48]. Substitution of the aqua ligand in **C1** with softer P-based ligands, the larger phosphorous atoms lead to longer Ru1-P1 bond lengths of 2.3122(5) Å (**C9**) and 2.3426(15) Å (**C10**), but still fall within expected ranges. In the case of phosphine-based donors, the observation of more electron-donating (ferrocenyl-based bis-phosphine *vs.* 4'-methoxyphenyl) phosphines gave rise to longer Ru1-P1 bond lengths. Steric bulk due to the incoming N- and P-donor ligands upon substitution had little effect on the structural features of the structures studied. The extra two co-crystallised water molecules in **C10** allow for an interesting hydrogen bonding network in three dimensions. A series of four water molecules exhibit intermolecular hydrogen bonds with one another, and in turn with four adjacent molecules of **C10** that extends along the *b*-axis (Figure S31). None of the other complexes exhibit hydrogen bonding interactions, nor do they exhibit π-π stacking interactions.

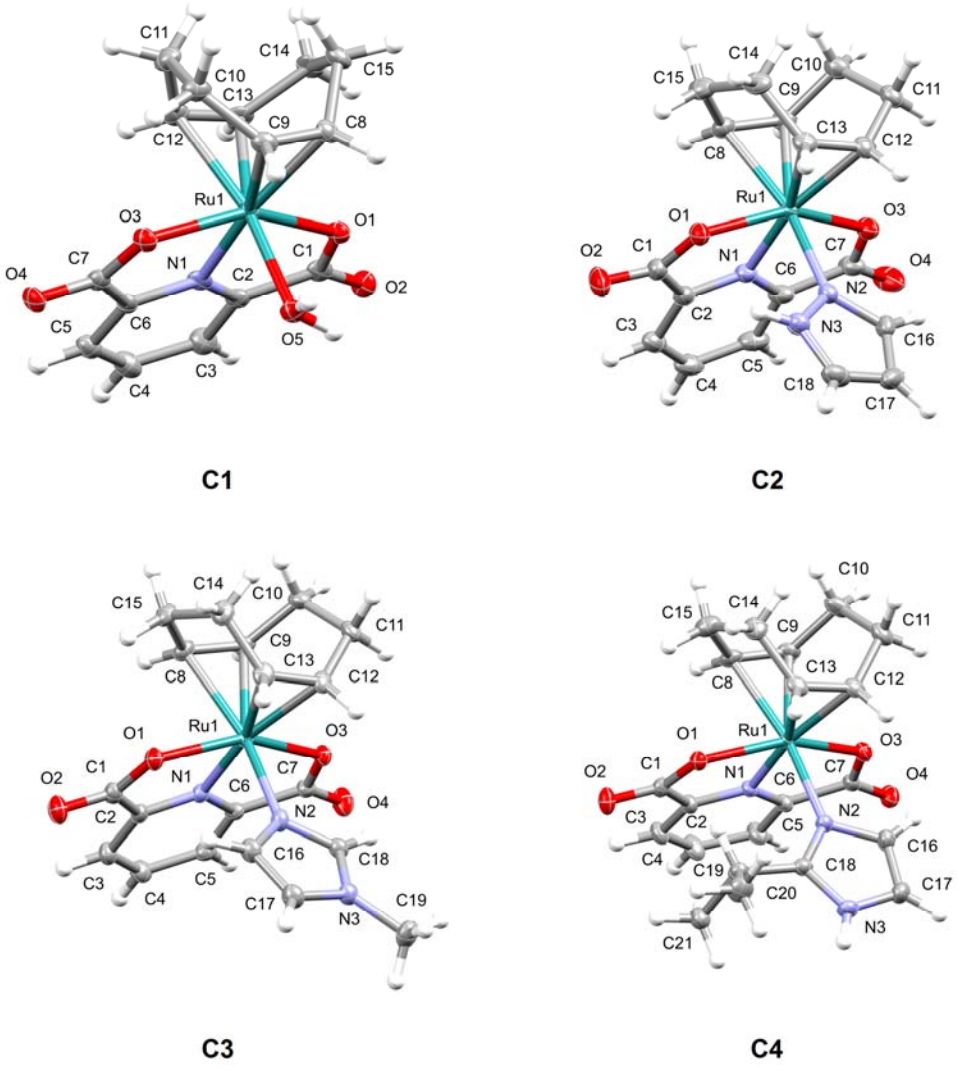

Figure 3. Molecular structures of complexes **C1**-**C4**. Thermal ellipsoids are drawn at 50% probability level. In this figure for complex **C1**, the polymorph **C1b** is represented. For structural comparisons between polymorphs **C1a**-**C1c**, please see the supplementary information.

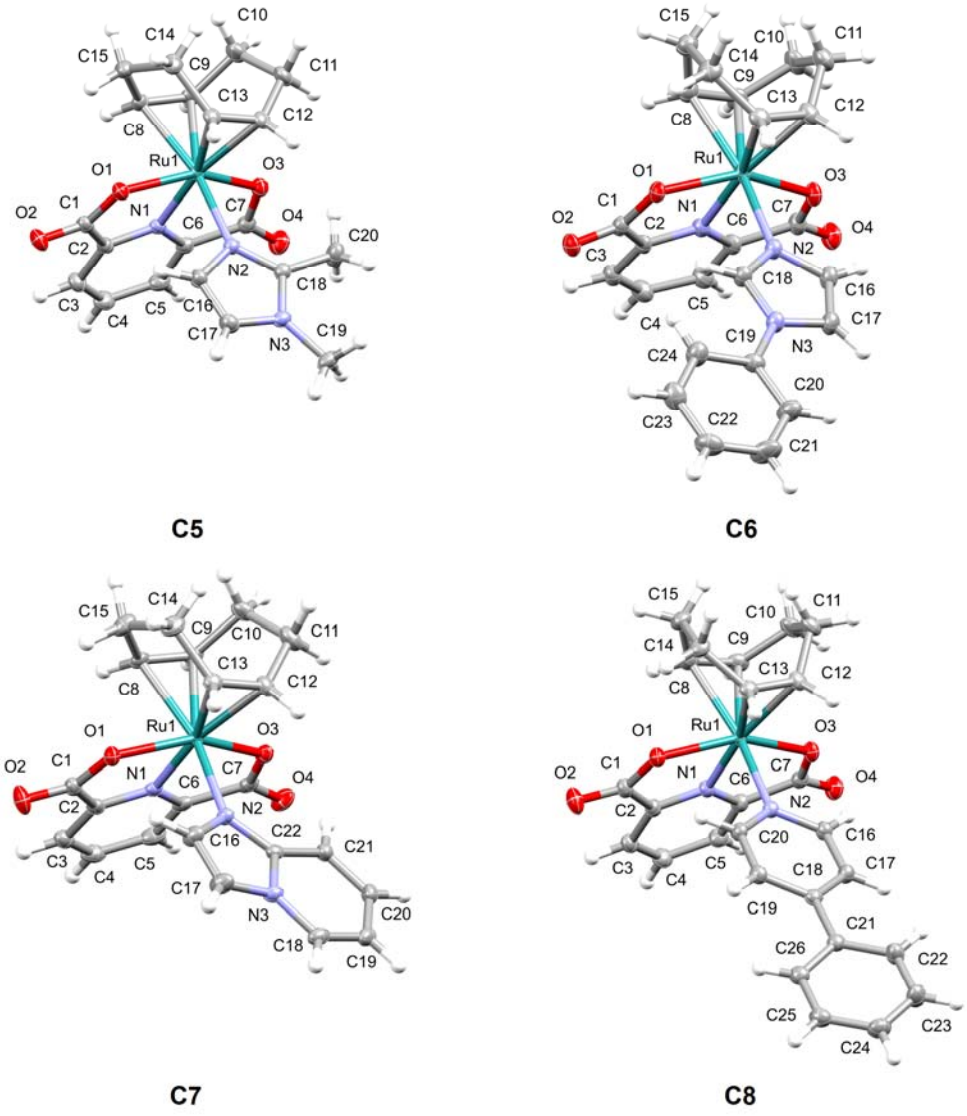

Figure 4. Molecular structures of complexes **C5**-**C8**. Thermal ellipsoids are drawn at 50% probability level.

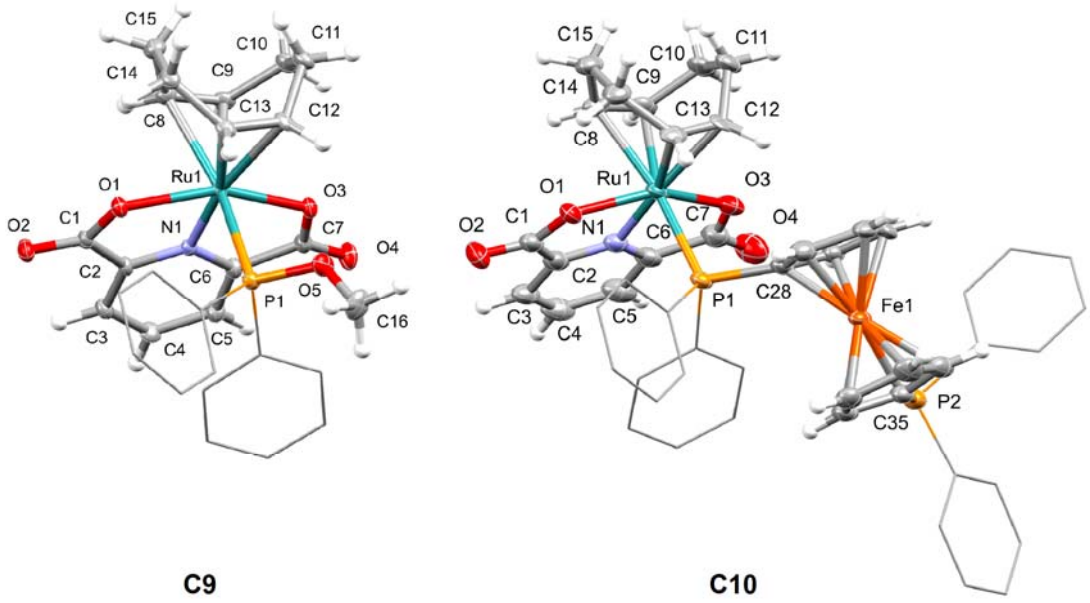

Figure 5. Molecular structures of complexes **C9** and **C10**. Thermal ellipsoids are drawn at 50% probability level. Phenyl moieties of the phosphine ligands are represented as wireframes, along with their protons hidden, both for clarity purposes. Two molecules of co-crystallised water in **C10** have been omitted for clarity.

Catalytic transfer hydrogenation

Transfer hydrogenation is a well-established green chemical transformation commonly employed in catalytic evaluation studies as a model hydrogenation reaction.[50] Several sectors including the flavour, fragrance, pharmaceutical, and biodiesel production industries have benefited from the remarkable efficiency, regio- and enantioselectivity of the transfer hydrogenation process.[50,51] In this part of the study the catalytic activity of complexes **C1**-**C10** featuring different nitrogen and phosphorus ancillary ligands are evaluated. The effect of the varied ligand systems on the catalytic activity of the respective complexes is of interest. The catalytic reaction was studied using a literature method[50] while using benzophenone (as substrate) and **C1** (as pre-catalyst) for method optimisation. The parameters optimised included reaction time, catalyst concentration, base, as well as temperature (Table 1). Reactions without the catalyst and/or base were also carried out (as control reactions) where in all three scenarios little to no organic product were obtained (entries 5-8

Table 1). As is typical in many related catalytic studies[50], the internal standard used was anisole while the hydrogen source was isopropanol. For solubility and catalyst stability reasons, reactions were conducted in C_6D_6 with the presence of ^{i}PrOH (300 µL), which also facilitated the direct analysis of the reaction mixtures using ^{1}H NMR spectroscopy. A catalytic amount of base (10 mol%) was required as an additive to facilitate activation of the pre-catalysts without which the catalytic reactions proved sluggish or fail to take place.

Table 1. Method optimisation and catalyst screening for the transfer hydrogenation of benzophenone.

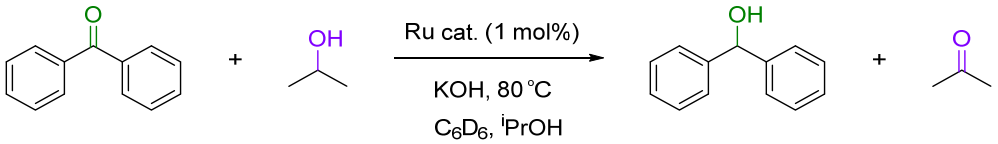

Entry	Complex	Catalyst conc. (mol%)	Temp. (^{o}C)	Base	Conversion (%)	Yield[a,b] (%)	TOF (h^{-1})[c]
1	**C1**	5[d]	80	KO^{t}Bu	98 (99)[e]	99 (99)[e]	(26)[e]
2	**C1**	3	80	KO^{t}Bu	94 (98)	94 (98)	63 (33)
3	**C1**	2	80	KO^{t}Bu	92 (94)	92 (94)	92 (47)
4	**C1**	1	80	KO^{t}Bu	78 (89)	78 (89)	156 (89)
5	**C1**	3	50	KOH	-	-	-
6	**C1**	3	RT	KOH	-	-	-
7	**C1**	-	80	-	-	-	-
8	**C1**	5	80	-	0 (0)	0 (0)	0 (0)
9	**C2**	1	80	KOH	1 (3)	1 (3)	2 (3)
10	**C3**	1	80	KOH	1 (1)	1 (1)	2 (1)
11	**C4**	1	80	KOH	73 (84)	73 (84)	146 (84)
12	**C5**	1	80	KOH	96 (96)	96 (96)	192 (96)
13	**C6**	1	80	KOH	43 (47)	43 (47)	86 (47)
14	**C7**	1	80	KOH	47 (60)	47 (60)	94 (60)

15	**C8**	1	80	KOH	0 (1)	0 (1)	0 (1)
16	**C9**	1	80	KOH	21 (29)	21 (29)	42 (29)
17	**C10**	1	80	KOH	70 (79)	70 (79)	140 (79)

General conditions: Ph_2CO (0.3 mmol, 0.6mmol[d]), anisole (0.3 mmol), ^{i}PrOH (300 µL), catalyst (1 mol %), C_6D_6, 80 °C, 1 h, KOH (10 mol%). [a] Conversion and yield based on the internal standard (anisole) after 30 minutes. [b] Parentheses indicate corresponding values after one hour. [c] Final TON values (1 hour) correspond to the TOF values indicated in parentheses. [e] Parentheses indicate corresponding values after 45 minutes.

Potassium hydroxide provided higher conversions as compared to potassium *tert*-butoxide (entries 1-4), presumably since the enhanced nucleophilicity and accessibility of the hydroxide anion (as compared to tert-butoxide anion) play an important role. Temperature studies showed that the optimum temperature for this catalytic study is 80^{o}C. The reaction was also performed at room temperature and 50^{o}C leading to almost no conversion (even with increased catalytic loadings of 3 mol%, entries 5-6). A reaction time profile revealed that the reaction at the otherwise optimised conditions required only an hour to achieve 99 % conversion (entry 1). In terms of catalyst concentration, 1 mol% was selected as the optimum, although slightly better yields of the product were obtained with 3 mol% catalytic loading. For economic and sustainability reasons, the lower catalyst concentration was selected, especially given the small difference in conversion between the two concentrations. Each of the remaining ruthenium complexes **C2**-**C10** were screened after obtaining the optimum conditions using benzophenone as substrate. The catalytic screening for each complex was generally carried out over 1 hour every 30 minutes to monitor performance. Complex **C5** featuring the *N*-methyl imidazole ligand was seen to perform the best (96 % yield after 1 hour) as compared to **C2** (pyrazole, 3 % yield), **C4** (imidazole-based,84 % yield), **C7** (imidazo-pyridine, 60% yield), **C8** (pyridine-based, 1 % yield), and **C9**-**C10** (phosphine-based, 29-79 % yield, entries 16-17). The solubility and (*in situ*) stability of the complexes have a notable effect on their associated catalytic performances. It was noted that complexes with a higher solubility (**C5**) in C_6D_6 perform better than those with lowered solubilities. It is interesting to note that **C3** and **C5** differs with the presence/absence of one CH_3 group, and **C4** and **C5** with a secondary CH group, yet **C3**-**C5** all differ noticeably in catalytic activity (entries 10-12). The enhanced activity of **C5** is ascribed to the perfect combination of the stronger donor ability of the 1,2-dimethylimidazole to better stabilise sensitive catalytic intermediates. Comparable activities were observed in reactions with **C1** (1 mol%, 89%, entry 4) using only pure ^{i}PrOH (91%), as well as doubling the concentration of ^{i}PrOH in C_6D_6 (88%, see

supplementary information). A series of carbonyl containing compounds with different substituents were screened using the best catalyst (**C5**) and our optimum conditions. It was observed that the substrate conversions were significantly affected by the functional groups present in each case.

For the substrate screening (Table 2), the ketone-containing substrates were found to be more selectively and efficiently converted (up to 96% conversion, entries 1-4 and 6) as compared to the aldehyde-containing substrates (entries 5 and 7). Substrates with electron-donating groups were efficiently converted as opposed to those with electron-withdrawing groups (entries 1 and 4 versus entries 6 and 7). The carbonyl substrates with electron withdrawing groups did not favour product formation (entries 7, 8, 12), whereas the aldehyde substrates with electron donating groups favoured product formation in moderate yields (entries 5 and 6). This indicates that substrates within the two groups (ketones and aldehydes) featuring electron-donating groups, such as $-CH_3$ or $-OCH_3$, are converted more efficiently than those with electron-withdrawing groups like $-NO_2$ (entries 1 and 4 *vs.* entries 6 and 7). This trend can be attributed to the increased electron density at the carbonyl carbon due to electron-donating substituents, which makes the carbonyl group more susceptible to nucleophilic attack during the catalytic cycle. As indicated in the caption of Table 2, several substrates failed to convert to their corresponding alcohols which primarily contained electron-withdrawing groups. Substrates containing -OH groups may also have hindered catalytic conversion by means of interaction with the metal center in a β-diketonato fashion. Substrate steric bulk also played a role where those containing bulky substituent groups were more efficiently converted (entries 1-4). Steric bulk observed in benzophenone (96% yield, entry 1) and acetonaphthone (85% yield, entry 4) may have been responsible for high conversions and yields seen. The greater the degree of steric bulk, the higher the conversions and yields observed. ^{1}H NMR spectra obtained of the reaction mixtures using **C1** indicated the presence of Ru-H species at -3.03 ppm which is typical of an inner-sphere mechanism (see supporting information). Two likely possibilities exist: (i) the pdc ligand becomes bidentate through which a carboxylate pendant group becomes the corresponding carboxylic acid along with the coordination of a hydride to the Ru center, *i.e.* [RuH(pdcH)(COD)(OH_2)]; (ii) the aqua ligand dissociates and allows for the coordination of a hydride ligand, making the resultant species anionic which is then stabilised by surrounding K^+ cations, *i.e.* K[RuH(pdc)(COD)]. At this stage, option (i) is ruled out due to the absence of a carboxylic acid proton in the same ^{1}H NMR spectrum where the hydride signal appears.

Table 2. Substrate screening for the transfer hydrogenation using **C5** as the catalyst.

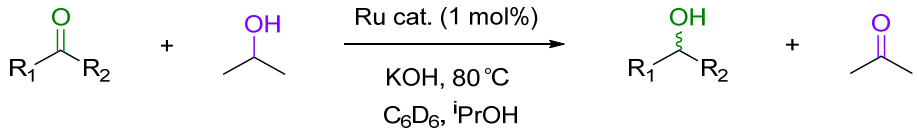

Entry	Substrate	Catalyst conc. (mol%)	Temp. (°C)	Base	Conv.[a] (%)	Yield[a] (%)	TON[b] (h^{-1})	TOF[b] (h^{-1})
1	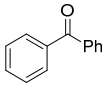	1	80	KOH	96	96	96	96
2		1	80	KOH	71	71	71	71
3		1	80	KOH	77	77	77	77
4	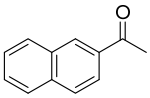	1	80	KOH	85 (100)[c]	85 (100)[c]	85(100)[c]	85(50)[c]
5	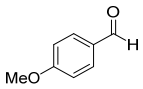	1	80	KOH	56(73)[d]	56(73)[d]	56(73)[d]	56(3.3)[d]
6	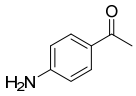	1	80	KOH	31(31)[e]	31(31)[e]	31(32)[e]	31(8)[e]
7	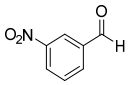	1	80	KOH	(5)[f]	5(5)[f]	5(6)[f]	5(2)[f]

General conditions: Ph_2CO (0.3 mmol), anisole (0.3 mmol), ^{i}PrOH (300 µL), catalyst (1 mol %), C_6D_6, 80 °C, 1 h, KOH (10 mol%). [a] Conversion and yield based on the internal standard (anisole) after 1 hr. [b] Final TON/TOF values (1 hour). [c] Conversion and yield after 2 hr. [d] Conversion and yield after 22 hr. [e] Conversion and yield after 4 hr. [f] Conversion and yield after 3 hr. Substrates that provided no conversion (even after 4 hours) included: phenacylbromide, 4'-hydroxyacetophenone, 2'-NO_2-acetophenone, 4'-NO_2-acetophenone, 2,2',4,4'-tetrahydroxybenzophenone, 3-hydroxybutan-2-one.

Electrochemical study

The electrochemical properties of 0.001 mol.dm^{-3} **C2-C10** were investigated in dry dichloromethane (DCM) at 25 °C using 0.1 mol.dm^{-3} [NBu_4][PF_6] as supporting electrolyte under an inert atmosphere. The poor solubility of **C1** in DCM necessitated the use of dichloroethane (DCE) at 70 °C to collect cyclic voltammetry data. Figure 6A shows the CV and linear sweep voltammetry (LSV) of **C2** in the presence of ferrocene (HFc, as the internal reference) and the CV at varied scan rates (without HFc). The LSV of **C2** *vs* ferrocene as internal standard confirmed a 1:1 ratio of 1-electron oxidations of Fe(II)/Fe(III) as well as the subsequent Ru(II)/Ru(III) redox couple (the concentrations were identical), which implies that the Ru(II)/Ru(III) redox couple is involved in a one electron transfer process. It can be assumed that the Ru(II)/Ru(III) redox couple for **C1-C10** is also a one electron process.

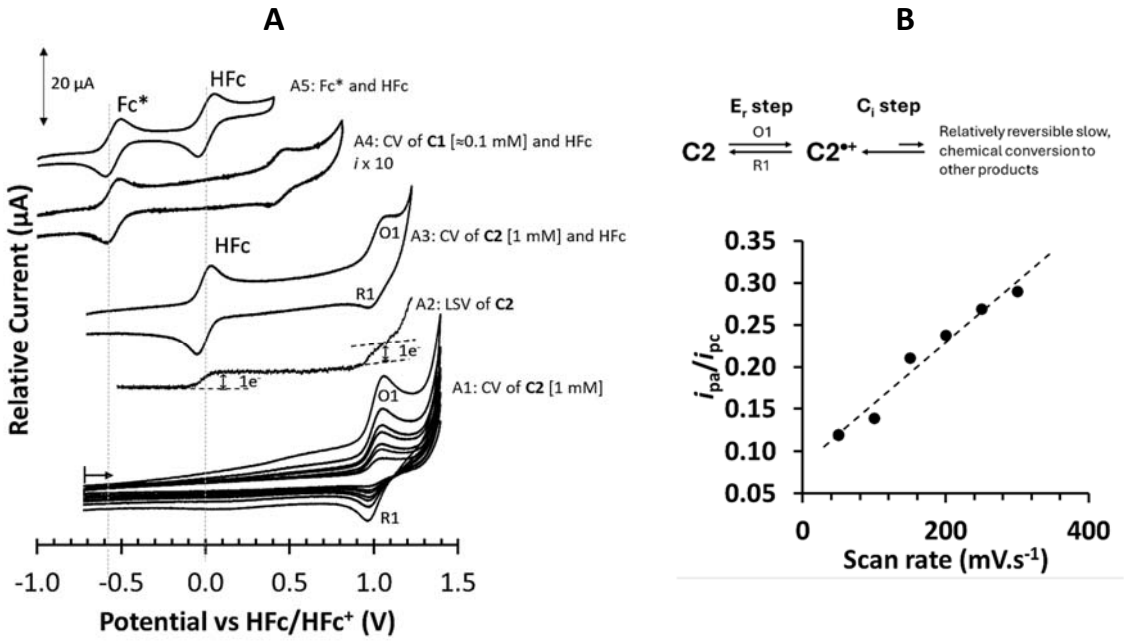

Figure 6. (A) A1: The CV (at different scan rates ranging from 50, 100, 150, 200, 250, 300 to 500 mV.s^{-1}) of **C2** (0.001 mol.dm^{-3}). A2: The Linear Sweep Voltammetry (LSV) of **C2** (0.001 mol.dm^{-3}). A3: The CV of **C2** (0.001 mol.dm^{-3}) and ferrocene (HFc) (as an internal reference) measured at a scan rate of 500 mV.s^{-1}. All measurements of **C2** were conducted in 0.3 mol.dm^{-3} [NBu_4][PF_6]/DCM on a glassy carbon working electrode at 25 °C. A4: The CV of an unknown concentration of **C1** (*ca.* 0.0001 mol.dm^{-3}) in DCE with Fc* (as an internal reference) with 0.067mM [NBu_4][PF_6] measured on a glassy carbon working electrode at 25 °C. A5: The CV of ferrocene (HFc) vs decamethyl ferrocene (Fc*). (B) The relationship between i_{pc}/i_{pa} and scan rates for the CV of **C2** in A1.

The peaks separation (ΔE) for scan rate below 500 mV.s^{-1} exhibited 70 < ΔE < 90 mV, which implies electrochemical reversibility for **C2**. The electrochemical process occurring at O1/R1 for **C2** is chemically irreversible, since the oxidation/reduction current (i_{pc}/i_{pa}) significantly deviates from unity. When increasing the scan rate between 50 and 1000 mV.s^{-1}, it was found that the i_{pc}/i_{pa} was not constant. As the scan rate increased, the i_{pc}/i_{pa} value decreased, with i_{pc}/i_{pa} = 0.12 at 50 mV.s^{-1} and i_{pc}/i_{pa} = 0.36 at 1000 mV.s^{-1} (see Figure 6B). This behaviour aligns with an E_rC_i mechanism, where the 'E_r' denotes an electrochemically reversible step and the 'C_i' a chemically irreversible step.[52] Following this, an additional electrochemical process occurs. In this mechanism, the oxidised product **C2**$^{\bullet+}$ formed during oxidation (O1, Figure 6A) is reversibly reduced (peak R1) to regenerated **C2**. However, **C2**$^{\bullet+}$ also slowly and irreversibly decomposes chemically (eq1, in Figure 6B). As the scan rate increases, there is less time for the oxidised species **C2**$^{\bullet+}$ to decompose before it undergoes reduction during the reverse (cathodic) half-cycle of the CV. Consequently, at higher scan rates a greater amount of **C2**$^{\bullet+}$ remains available for electrochemical reduction during the reverse CV cycle. This type of E_rC_i mechanism was found for the Ru-metal centre for all the compounds **C2-10**.

The cyclic voltammograms (scan rate of 100 mV.s^{-1}) of the Ru(II) complexes **C1-C10** are shown in Figure 7 and Figure 8 (see supplementary information for the varied scan rates and i_{pc}/i_{pa} vs graphs for **C2-C10**). A summary of the electrochemical data at 100 mV.s^{-1} is shown in Table 3 (see supplementary information for the data of the varied scan rates). The complexes **C1**-**C10** exhibited either one (**C1**-**C8**), two (**C9**) or three (**C10**) (red)ox events. The electrochemical process at *ca.* 0.894 V (for **C2-C8**) and *ca.* 0.364 V (for **C9** and **C10**) marked as O1 in Figure 7 is associated with the oxidation and reduction of the Ru-metal center. **C1**, the precursor complex to **C2**-**C10**, has an $E^{\circ'}$ = 0.424 V (*vs* HFc/HFc^{+}) for the Ru electron transfer process. Upon substitution of the aqua ligand for different N-donor ligands, the $E^{\circ'}$ increased on averaged *ca.* 0.52 V. This indicates that the ligand **L2-L8** are more electron withdrawing than the aqua ligand, causing the Ru to get reduced at higher potentials. As phosphine ligands are known to be stronger electron donors than aqua ligands[53], they effectively increase electron density at the Ru center, leading to a decrease in the oxidation potential $E^{\circ'}$. This shift in $E^{\circ'}$ aligns with the expected electron donating influence of the phosphine ligands on the metal center (Figure 7 and Table 3). The order of increasing reduction potential for the complexes is: **C9** (0.361 V) < **C10** (0.366 V) < **C5** (0.840 V) < **C7** (0.846 V) < **C4** (0.861 V) < **C3** (0.889 V) < **C6** (0.927 V) < **C8** (0.989 V) < **C2** (1.009 V). When comparing the reduction potentials ($E^{\circ'}$) of **C2-C10** with the yields of the transfer hydrogenation (Table 1), it was found that in most cases as the $E^{\circ'}$ decreased, the corresponding organic product yield increased. For instance, **C1** had lower $E^{\circ'}$ but gave the highest yield after 45 minutes of reaction. **C2** and **C3** had high values of $E^{\circ'}$ but gave lower yields of product.

C5 is an exception, despite its moderately high $E^{\circ\prime}$, the product yield was still high. This could potentially be ascribed to the Ru-metal center that can either more efficiently transfer electrons to the substrate due to the lower $E^{\circ\prime}$, or the Ru's ability to transfer "hydrogen" more easily to the substrate, and as a result lower the overall activation energy of the catalysis process. It is important to note that regardless of the mechanism at play (inner-sphere or outer-sphere mechanism), the formal oxidation state of Ru^{2+} is not expected to change during catalysis, and therefore the ability of the metal center to rely on the ancillary ligands to efficiently help with the transfer of "hydrogen" from isopropanol remains the key to its associated catalytic activity.

Table 3. Electrochemical data (*vs.* ferrocene) of redox processes observed for **C1**–**C10**.

	$E_{pa\ O1}$ (V)	$E_{pc\ R1}$ (V)	$E^{\circ\prime}$	ΔE	i_{pa} (µA)	i_{pc} (µA)	i_{pa}/i_{pc}
C1	0.463	0.385	0.424	0.078	0.32	0.24	0.71
C2	1.047	0.97	1.009	0.077	10.29	1.43	0.14
C3	0.929	0.849	0.889	0.080	6.83	4.17	0.61
C4	0.891	0.832	0.861	0.059	7.00	4.00	0.57
C5	0.876	0.805	0.840	0.071	5.50	2.25	0.41
C6	0.964	0.890	0.927	0.074	5.45	2.73	0.50
C7	0.890	0.802	0.846	0.088	5.17	2.50	0.48
C8	1.034	0.944	0.989	0.090	10.45	1.82	0.17
C9 $_{O1/R1}$	0.361	0.312	0.337	0.049	0.73	0.60	0.82
C9 $_{O2/R2}$	0.919	0.856	0.888	0.063	3.75	0.13	0.03
C10 $_{O1/R1}$	0.366				2.26		
C10 $_{O2/R2}$	0.643	0.547	0.595	0.096	4.33	2.88	0.66
C10 $_{O3/R3}$	0.870	0.727	0.799	0.143	1.90	1.00	0.53

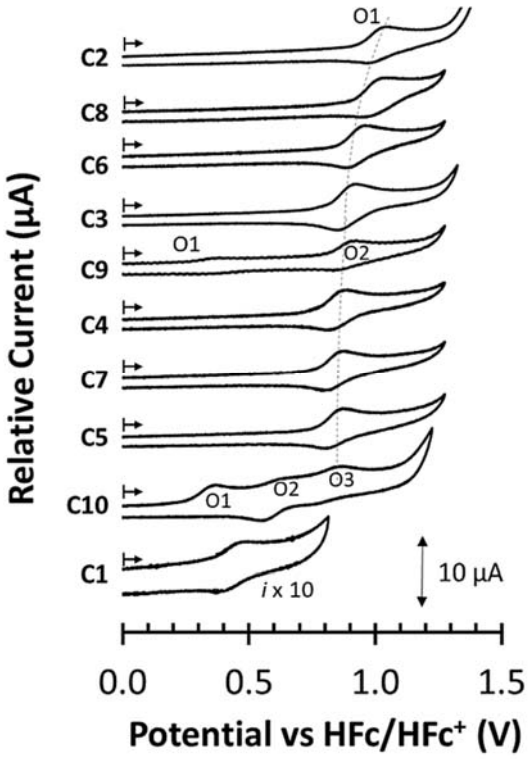

Figure 7. Comparative cyclic voltammograms of **C2**-**C10** (and **C1** in DCE with 0.067mM $[NBu_4][PF_6]$) *vs* ferrocene using a scan rate of 100 $mV.s^{-1}$. CVs were measured in 0.3 $mol.dm^{-3}$ $[NBu_4][PF_6]$/DCM on a glassy carbon working electrode at 25 °C. [Ru] = 0.001 $mol.dm^{-3}$ or saturated solution. Scans were initiated in the positive direction.

While complexes **C1**-**C8** all exhibited one redox wave in the oxidation window, complexes phosphine-containing complexes **C9** and **C10** exhibited additional redox waves in Figure 7 and CVs in the Supporting information. The additional red(ox) events (O2 for **C9** and O3 for **C10**) are reasoned to be due to the oxidation of the phosphinite or phosphine ligand.[54] This event is electrochemically reversible in **C9** (ΔE = 0.063 V, $E^{o'}$ = 0.888 V), and electrochemically irreversible for the phosphine ligand in **C10** (ΔE = 0.143 V, $E^{o'}$ = 0.799 V). Another redox event for **C10** was observed at $E^{o'}$ = 0.595 V marked O2/R2 in Figure 7 and the CV in the supporting information. The origin of this redox event is proposed due to the presence of the ferrocene moiety in the phosphine ligand (in accordance with literature of free PPh_2Fc), and therefore refers to the Fe(II)/Fe(III) redox wave.[55] The CVs of **C2**-**C10** also revealed a chemically and electrochemically irreversible reduction event at *ca.* -1.732 V (*vs* Ag/Ag^+), which is associated with the electron uptake *via* a ligand (Figure S35 in the Supporting

Information). The associated LSV of **C2** (Figure S35) suggests a 1:1 ratio of 1-electron reductions of Fe(III)/Fe(II), followed by a ligand-based reduction.

Computational details

For a clear understanding of the electrochemical origin of both the first oxidation and reduction processes for the complexes containing pdc backbone and COD ligand, DFT studies of all complexes were conducted. Using **C5** as representative example, selected frontier molecular orbitals of **C5** are shown in Figure 8. As a starting point, the global minimum conformations of each complex were obtained by full geometry optimisation (with zero imaginary frequencies), using the obtained crystal structures as input. The respective conformers (lowest energy, gas phase calculated) obtained, closely corresponded in all cases to the experimentally observed conformers (solid state, from SCXRD). From these results, it is expected that the HOMO of the neutral complex and LUMO of the corresponding oxidised species should collectively hint to the origin of the first oxidation process. This is proposed because the oxidation process involves the removal of an electron from the HOMO of the neutral complex. The subsequent one-electron reduction of the cation is proposed to be Ru-based whereby Ru^{3+} is reduced back to Ru^{2+}. Considering the frontier orbitals of the cation and neutral species (Figure 8), the LUMO of the cation and HOMO of the neutral species indeed correlate well to indicate the same locus of the reduction event. For the first electron reduction of neutral **C5**, the LUMO of the neutral complex and the HOMO of the corresponding reduced species are expected to indicate the origin of the first reduction process. For the first electron oxidation of the neutral complex **C5**, a clear correlation between the HOMO (neutral complex) and the LUMO (oxidised species) indicates that the first oxidation process is Ru-based, with the metal oxidised from Ru(II) to Ru(III). For the reduced specie, the electron density of the HOMO is centred mainly on the pdc ligand, which now correlates with the LUMO of the neutral complex. These results agree with our experimental electrochemistry observations in that the first electron reduction is primarily ligand-based, and the first electron oxidation, followed by a subsequent reduction is associated with the Ru^{II}/Ru^{III} redox couple.

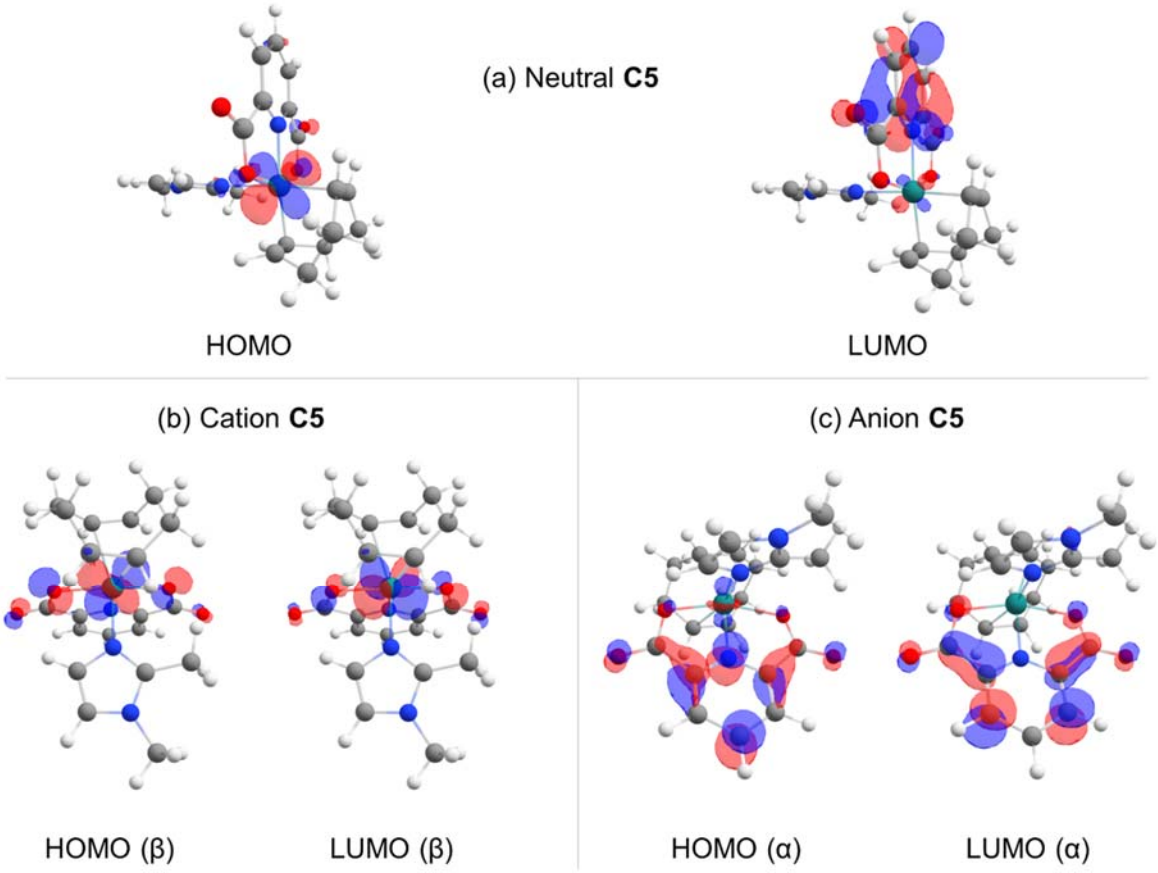

Figure 8. Selected molecular (frontier) orbitals indicated in red and blue of **C5**: (a) neutral, (b) cation (+1, after 1é removal), and (c) anion (-1, after 1é addition). α = alpha spin of electrons, β = beta spin of electrons.

To gain more insight into the relevant reactivities/stabilities of the complexes investigated, the molecular orbital energies of complexes **C1**-**C10** were plotted (Figure 9), and corresponding energy gaps (energy difference between the frontier orbitals, thus E_{LUMO}-E_{HOMO}) were calculated. The change in ancillary ligand (N- or P-donor), as well as a change in functional group(s) among the N-donor ligands appear to have a limited effect on the resulting energy gap of the corresponding complexes, where the energy gaps of **C1**-**C10** all appeared within a narrow range of 3.898-4.173 eV. These values correlate with related Ru(II) compounds calculated using similar computational treatment methods (B3LYP, def-tzvpp).[56,57] A smaller energy gap is usually associated with less stability, or conversely increased reactivity with an associated complex. From Figure 9 complex **C1** (and in fact the majority of N-donor pyrazole and imidazole-based ligands) are associated with the largest energy gaps, and hence most stable (or least reactive) complex, whereas complex **C10** (featuring the mono-coordinated

bisphosphine) was predicted to be the least stable (or most reactive) complex. Notably, the calculated energy gaps all fall within a narrow range and do not necessarily translate to the experimentally observed behaviour (within experimental error) of the respective complexes. From our observations, all complexes were air- and moisture stable in the solid state for months without any noticeable signs of decomposition.

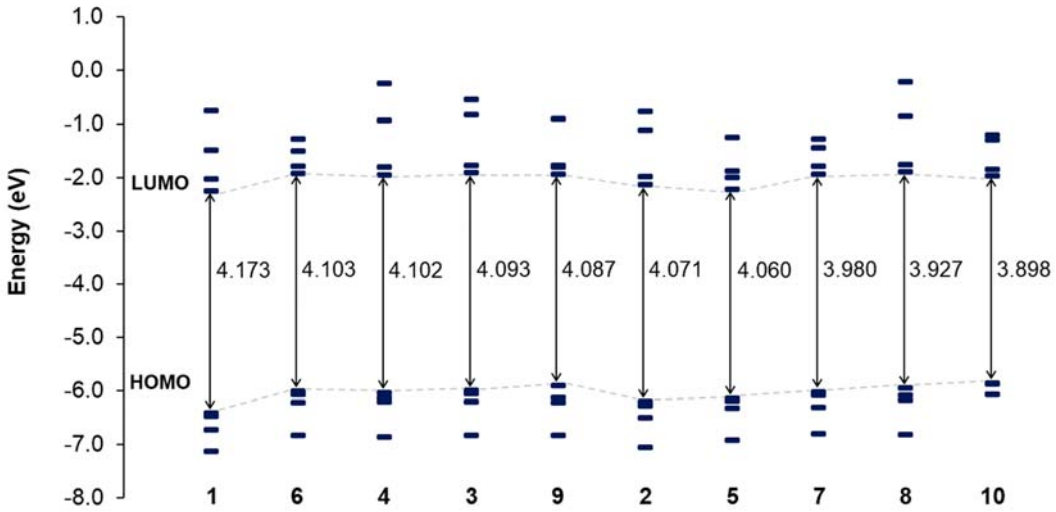

Figure 9. Molecular orbital energy levels (eV) of complexes **C1**-**C10**.

Table 4. DFT calculated adiabatic ionisation potential (IP, eV) and adiabatic electron affinity (EA, eV) values for complexes **C1**-**C10**.

Complex	IP (eV)	EA (eV)
1	7.18	1.82
2	7.00	1.05
3	6.74	0.83
4	6.71	0.88
5	6.68	0.79
6	6.71	0.94
7	6.68	0.94
8	6.77	1.31
9	6.53	0.74
10	6.57	0.95

In Table 4, the adiabatic electron affinity (EA) and ionisation potential (IP) values were calculated based on the DFT-obtained data. The EA values are calculated as the difference between the energy of the neutral complex (n electrons) and the mono-reduced (n + 1 electrons) species. Similarly, the IP values are calculated from the difference between the neutral complex and the mono-oxidised (n – 1 electrons) species. The calculated IP and EA values lie within a comparable range between the different complexes with 0.65 eV (IP) and 1.08 eV (EA). These two parameters collectively suggest an effect of the change of ligand within each complex and the resulting energy required to either oxidise or reduce the complex. In general, it was noted that with increasing IP and EA values, the experimentally measured reduction potential ($E^{o'}$) also increased for **C2-C10**. Conradie[58] found in their tris(β-ketoiminato)-based Ru(III) complexes IP values of 5.59-5.83 eV, and EA values of 1.15-1.62 eV. The same group[59] also found that for tris(phenantroline) and tris(bipyridine) derivative complexes of Ru(II), the corresponding IP and EA values can rise to values as high as 10.29-13.40 eV and 5.46-8.38 eV, respectively. Considering the Principle of Maximum Hardness (PMH) with respect to molecular orbital (MO) theory, the hardness of a molecule (η) is essentially defined as half the magnitude of the energy gap of the molecule.[60] The energy gap is the absolute value of the energy difference between the HOMO and the LUMO of the (neutral) molecule. Within a given chemical system, the tendency to maximise the hardness of its respective molecules therefore exists since a hard molecule tends to have a large energy gap.[60] Comparison of the hardness of complexes **C1**–**C8**, the same trend is observed: all complexes ($2.09 \leq \eta \leq 1.95$) exhibit relatively hard character and are therefore expected to be stable under ambient conditions.

Conclusion

A series of nine novel ruthenium-ONO complexes with different N- and P-donor ancillary ligands were synthesised and thoroughly characterised by NMR spectroscopy, mass spectrometry, elemental analysis, and single-crystal X-ray diffraction (SCXRD). The synthetic procedure is straightforward and does not require strict moisture- or oxygen-free conditions. These complexes demonstrated variable catalytic efficiency as pre-catalysts in the transfer hydrogenation of carbonyl-containing compounds, achieving up to 100% yields in some cases. Notably, complex **C5** showed superior catalytic activity, attributed to its enhanced electron density at the Ru center (signalled by its low reduction potential), thereby facilitating the hydrogen transfer process. In contrast, complexes **C2**, **C3**, and **C8** exhibited only minimal activity (yields of 1–3%), which correlates with their higher reduction potentials and likely indicates reduced electron density availability at the metal center for catalytic activation. Complex **C1** displayed high activity, likely due to the facile dissociation of its aqua ligand, which creates an accessible coordination site crucial for catalytic turnover. This observation highlights the

importance of (hemi)labile ligands in the catalytic cycle, particularly for facilitating the formation of vacant coordination sites, a known requisite for effective catalysis in transition metal complexes. Electrochemical studies revealed a one-electron reversible Ru^{II}/Ru^{III} redox couple across the complexes, with additional redox events in the phosphine-containing complexes **C9** and **C10**, indicating the influence of P-donor ligands on the redox behaviour. The chemically irreversible reduction of the ligand observed at anodic potentials across all complexes emphasises the stability and resilience of these ligands under oxidative conditions. Density functional theory (DFT) calculations further supported these findings, identifying metal-centered oxidation and ligand-centered reduction as primary pathways, which could guide the rational design of new Ru complexes with tailored electronic- and steric properties for optimised catalytic performance. These findings provide valuable insights into the possible structure-activity relationships governing the catalytic performance of ruthenium-ONO complexes. By correlating redox properties and ligand lability with catalytic efficiency, this study establishes a foundation for the targeted development of ruthenium-based catalysts with potential applications in sustainable hydrogenation processes.

Experimental Section

General Considerations

Complex syntheses were carried out under inert conditions using standard Schlenk techniques.[61] All reagents and solvents were purchased from commercial suppliers and there was no need for further purification. The polymeric complex $[RuCl_2(COD)]_x$ was synthesised using a published method.[57] The new complexes were synthesised using an already established synthetic protocol[48] with minor modification as outlined below. Gravity column chromatography (elution with CH_2Cl_2/acetone 1:1) was used for purification where necessary. ^1H (300/400 MHz), ^{13}C (75.5/100.6 MHz), ^{31}P (162 MHz) NMR spectra were recorded on either a Bruker Avance-400 or a Bruker Gemini 300 spectrometer using $CDCl_3$, unless otherwise stated. Chemical shifts were referenced to the internal residual solvent resonances (7.24 ppm (^1H NMR), 77.0 ppm (^{13}C NMR)). Electrospray mass spectra (ESI-MS) were recorded on a Micromass Quatro LC instrument. Acetonitrile or methanol (**C4**) were used as the solvent for analysis using the positive ionisation electrospray technique. EA analyses were performed at UKZN using a ThermoScientific Flash2000 Elemental Analyser.

Synthesis of C1

A round bottom flask with MeOH (40 mL), dipicolinic acid (0.73 g, 4.38 mmol) and KOH (0.63 g, 11.19 mmol) was stirred for 15 minutes. Afterwards, $[RuCl_2(COD)]_x$ (1.00 g, 3.61 mmol per mol Ru) was added

and left to heat under reflux overnight. $AgNO_3$ solution (0.73g in 2ml H_2O) was added to the mixture and the reaction was allowed to stir for 2hours. The reaction mixture was filtered upon which the filtrate was concentrated *in vacuo*. The residue was washed with water and acetone to give a yellow solid in 71% yield (0.99 g, 2,37 mmol). The ^1H and ^{13}C NMR spectra obtained correspond to that of Xie *et al.*[48]

General synthesis of C2-C10

Complex **C1** (0.1g, 1mmol) and ligand (**L1**-**L9**, 2mmol) were heated under reflux in MeOH (15 mL) under an argon atmosphere in a Schlenk tube overnight. The crude mixture was further purified either by gravity silica gel column chromatography using gradient elution (Acetone as eluent for **C9**) and (DCM/Acetone 1:1 as eluent for **C10**)) and/or solvent wash (ethyl acetate; **C2**-**C8**) as appropriate.

C2: Yield 99%. ^1H NMR (300 MHz, $CDCl_3$) δ_H 11.02 (s, 1H, NH of pyrazole), 8.07 (d, *J* = 7.7 Hz, 2H, CH of pdc), 7.95-7.90 (m, 1H, CH of pdc), 7.62 (d, *J* = 2.1, 0.7 Hz, 1H, CH of pyrazole), 7.53 (d, *J* = 2.5, 1.6, 0.8 Hz, 1H, CH of pyrazole), 6.30 (m, 1H, CH of pyrazole), 4.47 (m, 2H, CH of COD), 3.53 (m, 2H, CH_2 of COD), 2.27-2.64 (m, 8H, CH of COD). ^{13}C NMR (300 MHz, $CDCl_3$) δ_C 172.19 (CO of pdc), 149.35 (CCH of pdc), 139.67 (CH of pdc), 136.67 (CH of pyrazole), 130.49 (CH of pyrazole), 127.68 (CH of pdc), 107.25 (CH of pyrazole), 100.42 (CH of COD), 93.79 (CH of COD), 29.44 (CH_2 of COD). HR-MS (ESI) m/z 444.0239 calcd 444.02 ($[M+H]^+$). Elemental Analysis: calcd: (**C2**.0.5$CHCl_3$) C, 44.25; H, 3.91; N, 8.37; found: C, 44.7; H, 3.92; N, 8.11.

C3: Yield 54%. ^1H NMR (300 MHz, $CDCl_3$) δ_H 8.03 (d, *J* = 7.7 Hz, 2H, CCH of pdc), 7.96 – 7.70 (m, 1H, CCH of pdc), 7.48 (s, 1H, CH of imidazole), 7.01 (s, 1H, CH of imidazole), 6.72 (t, *J* = 1.4 Hz, 1H, CH of imidazole), 4.58 – 4.29 (m, 2H, CH of COD), 3.58 (s, 3H, CH_3 of imidazole), 3.53 – 3.44 (m, 2H, CH_2 of COD), 2.23-2.68 (m, 8H, CH of COD). ^{13}C NMR (300 MHz, $CDCl_3$) δ_C 172.07 (CO of pdc), 149.52 (CCH of pdc), 137.04 (CH of pdc), 136.11 (NCN of imidazole), 127.65 (CH of pdc), 127.30 (CH of pdc), 120.93 (CH of imidazole), 100.32 (CH of COD), 93.32 (CH of COD), 34.54 (CH_3 of methylimidazole), 29.44 (CH_2 of COD). HR-MS (ESI) m/z 458.0403, calcd 458.05 ($[M+H]^+$). Elemental Analysis: calcd: C, 49.99; H, 4.64; N, 9.21; found: C, 49.90; H, 4.69; N, 8.98.

C4: Yield 96%. ^1H NMR (400 MHz, $CDCl_3$) δ_H 9.96 (s, 1H, NH of imidazole), 8.07 (d, *J* = 7.7 Hz, 2H, CH of pdc), 7.88 (m, *J* = 8.1, 7.3 Hz, 1H, CH of pdc), 6.93 (t, *J* = 2.0 Hz, 1H, CH of imidazole), 6.76 (t, *J* = 2.1 Hz, 1H, CH of imidazole), 4.62 (m, *J* = 4.7, 1.9 Hz, 2H, CH of COD), 3.91 (m, *J* = 7.1 Hz, 1H, CH of imidazole),

3.40 (dt, *J* = 4.6, 1.9 Hz, 2H, CH of COD), 2.66-2.56 (m, 2H, CH_2 of COD), 2.56-2.38 (m, 4H, CH_2 of COD), 2.22 (m, *J* = 10.5, 8.2, 6.2, 3.4 Hz, 2H CH_2 of COD), 1.16 (d, *J* = 7.0 Hz, 6H, CH_3 of isopropylimidazole). ^{13}C NMR (400 MHz, $CDCl_3$) δ_C 172.0 (CO of pdc), 157.3 (CCH of pdc), 149.9 (NCN of imidazole), 136.2 (CH of pdc), 127.4 (CH of pdc), 125.6 (CH of imidazole), 115.4 (CH of imidazole), 101.5 (CH of COD), 92.4 (CH of COD), 29.4 (CH_2 of COD), 29.2 (CH_2 of COD), 26.3 (CH of isopropyl imidazole), 23.0 (CH_3 of isopropyl imidazole). HR-MS (ESI) m/z 486.1182, calcd 486.11 ($[M+H]^+$). Elemental Analysis: calcd (**C4**.0.25$CHCl_3$): C, 49.72; H, 4.76; N, 8.19; found: C, 49.82; H, 5.08; N, 8.03.

C5: Yield 93%. ^1H NMR (400 MHz, $CDCl_3$) δ_H 8.06 (d, *J* = 7.7 Hz, 2H, CH of pdc), 7.86 (m, *J* = 8.1, 7.3 Hz, 1H, CH of pdc), 6.93 (d, *J* = 1.8 Hz, 1H, CH of imidazole), 6.60 (d, *J* = 1.8 Hz, 1H, CH of imidazole), 4.63 (m, *J* = 4.8, 1.9 Hz, 2H, CH of COD), 3.46-3.39 (m, 5H CH3 of imidazole and CH of COD), 2.64-2.23 (m, 11H, CH_2 of COD and CH_3 of imidazole). ^{13}C NMR (400 MHz, $CDCl_3$) δ_C 171.8 (CO of pdc), 149.9 (CCH of pdc), 147.6 (NCN of imidazole), 136.1 (CH of pdc), 127.3 (CH of pdc), 125.5 (CH of imidazole), 120.1 (CH of imidazole), 101.3 (CH of COD), 92.2 (CH of COD), 33.7 (CH_3 of imidazole), 29.4 (CH_2 of COD), 29.2 (CH_2 of COD), 11.9 (CH_3 of imidazole). HR-MS (ESI) m/z 472.0562, calcd 472.06 ($[M+H]^+$). Elemental Analysis: calcd (**C5**.0.2$CHCl_3$): C, 49.08; H, 4.73; N, 8.50; found: C, 49.30; H, 4.74; N, 8.55.

C6: Yield 77%. ^1H NMR (300 MHz, $CDCl_3$) δ_H 8.07 (d, *J* = 7.7 Hz, 2H, CH of Pyridine), 7.92-7.86 (m, *J* = 15.5, 4.3 Hz, 2H, CH of pdc and CH of phenyl imidazole), 7.46 – 7.34 (m, 2H, CH of phenylimidazole), 7.26 – 7.22 (m, 4H, CH of phenylmidazole), 7.15 (t, *J* = 1.6 Hz, 1H, CH of pyrazole), 4.69 – 4.35 (m, 2H, CH of COD), 3.70 – 3.37 (m, 2H, CH of COD), 2.29-2.69 (m, 8H, CH of COD). ^{13}C NMR (300 MHz, $CDCl_3$) δ_C 172.1 (CO of pdc), 149.6 (CCH of pdc), 136.3 (CH of pdc), 135.9 (CCH of phenylimidazole), 135.1 (NCN of imidazole), 130.1 (CH of phenylimidazole), 128.7 (CH of phenylimidazole), 128.4 (CH of phenylimidazole), 128.3, (CH of phenylimidazole) 127.4 (CH of pdc), 121.4 (CH of imidazole), 119.1 (CH of imidazole), 100.5 (CH of COD), 93.4 (CH of COD), 29.5 (CH_2 of COD) HR-MS (ESI) m/z 520.0545 calcd 520.06 ($[M+H]^+$). Elemental analysis: calcd (**C6**.0.33$CHCl_3$): C, 52.35; H, 4.21; N, 7.53; found: C, 52.45; H, 4.48; N, 7.76.

C7: Yield 99% ^1H NMR (400 MHz, $CDCl_3$) δ_H 8.45 (dd, *J* = 9.5, 0.7 Hz, 1H, CH of phenyl), 8.04 (d, *J* = 7.7 Hz, 2H, CH of pdc), 7.98 (m, *J* = 6.8, 1.1 Hz, 1H, CH of phenyl), 7.84 (dd, *J* = 8.0, 7.5 Hz, 1H, CH of pdc), 7.60 (d, *J* = 1.8 Hz, 1H, CH of imidazole), 7.39 (d, *J* = 1.3 Hz, 1H, CH of imidazole), 7.29 (m, *J* = 9.5, 6.8, 1.3 Hz, 1H, CH of phenyl), 6.85 (m, *J* = 6.8, 1.0 Hz, 1H, CH of imidazole), 4.83 – 4.44 (m, 2H, CH of COD), 3.60 – 3.35 (m, 2H, CH of COD), 2.84 – 2.11 (m, 8H, CH_2 of COD). ^{13}C NMR (400 MHz, $CDCl_3$) δ_C 171.9 (CO of pdc), 149.8 (CCH of pdc), 145.4 (NCN of imidazole), 136.1 (CH of pdc), 130.6 (CH of phenyl),

127.4 (CH of pdc), 127.0 (CH of phenyl), 126.4 (CH of phenyl), 117.6 (CH of imidazole), 114.0 (CH of imidazole), 112.7 (CH of phenyl), 101.2 (CH of COD), 92.6 (CH of COD), 29.5 (CH_2 of COD), 29.4 (CH_2 of COD). HR-MS (ESI) m/z 494.0402 calcd 494.05 ($[M+H]^+$). Elemental analysis: calcd (**C7**.0.2$CHCl_3$): C, 51.76; H, 4.54; N, 8.23; found: C, 51.44; H, 4.41; N, 8.13.

C8: Yield 95%. ^{1}H NMR (300 MHz, $CDCl_3$) δ_H 8.62 (dd, *J* = 5.4, 1.4 Hz, 2H, CH of phenylpyridine), 8.08 (d, *J* = 7.7 Hz, 2H, CH of pdc), 7.89 (m, *J* = 8.2, 7.3 Hz, 1H, CH of pdc), 7.64 – 7.33 (m, 5H), 4.55 – 4.28 (m, 2H, CH of COD), 3.71 – 3.45 (m, 2H, CH of COD), 2.72-2.26 (m, 8H, CH_2 of COD). ^{13}C NMR (400 MHz, $CDCl_3$) δ_C 171.9 (CO of pdc), 149.8 (CH of phenylpyridine), 145.4 (CCH of pdc), 136.1 (CCH of phenylpyridine), 131.0 (CCH of phenylpyridine), 127.3 (CH of pdc), 127.1 (CH of phenylpyridine), 126.5 (CH of phenylpyridine), 117.6 (CH of phenylpyridine), 114.0 (CH of pdc), 112.8 (CH of phenylpyridine), 112.6 (CH of phenylpyridine), 101.2 (CH of COD), 92.6 (CH of COD), 29.5-29.4 (8H, CH_2 of COD). HR-MS (ESI) m/z 531.0590 calcd 531.06 ($[M+H]^+$). Elemental Analysis: calcd (**C8**.0.1$CHCl_3$): C, 57.89; H, 4.49; N, 5.17; found: C, 58.11; H, 4.69; N, 5.14.

C9: Yield 37%. ^{1}H NMR (400 MHz, $CDCl_3$) δ_H 7.79-7.70 (m, 3H, CH, pdc), 7.39-6.94 (m, 10H, phenyl), 5.23-5.15 (m, 2H, CH of COD), 4.23 (m, *J* = 2.4 Hz, 2H, CH of COD), 3.34-3.32 (d, *J* = 11.1 Hz, 3H, OCH_3), 2.82-2.56 (m, 4H, CH_2 of COD), 2.33-2.19 (m, 4H, CH_2 of COD). ^{13}C NMR (400 MHz, $CDCl_3$) δ_C 170.7 (CO of pdc), 149.3-127.2 (CH/CCH of phenyl and pdc), 121.0 (CH of COD), 87.0 (CH of COD), 55.0 (CH_3 of methyl diphenylphosphinite), 31.6 (CH_2 of COD), 27.3 (CH_2 of COD). ^{31}P NMR (100 MHz, $CDCl_3$) δ_P 125.6. HR-MS (ESI) m/z 592.0527 calcd 592.06 ($[M+H]^+$). Elemental Analysis: calcd (**C9**.0.14$CHCl_3$): C, 55.63; H, 4.67; N, 2.31; found C, 55.60; H, 4.78; N, 2.12.

C10: Yield 64%. ^{1}H NMR (300 MHz, $CDCl_3$) δ_H 7.60-7.14 (m, 23H of phenyl and pdc), 4.60-3.46 (10H, CH of COD and CH of DPPF), 2.65-2.11 (m, 8H, CH_2 of COD). ^{13}C NMR (300 MHz, $CDCl_3$) δ_C 170.8 (CO of pdc), 149.3-127.2 (CH/CCH of phenyl and pdc), 117.1-117.0 (CH of COD), 88.1 (CH of COD), 74.4-72.6 (CH of DPPF), 31.3 (CH_2 of COD), 27.7 (CH_2 of COD). ^{31}P NMR (100 MHz, $CDCl_3$) δ_P 27.6, -19.1. HR-MS (ESI) m/z 930.0710 calcd for 930.08 ($[M+H]^+$). Elemental Analysis: calcd (**C10**.0.25$CHCl_3$): C, 61.71; H, 4.55; N, 1.46; found: C, 61.50; H, 4.70; N, 1.50.

Procedure for catalytic transfer hydrogenation

The catalytic reactions were done in an NMR tube, affording us the ease of analysing the catalytic reactions. A tightly sealed NMR tube containing benzophenone (0.3mmol), anisole as an internal standard (0.3 mmol), isopropanol (300 µL), base (KOH, 10 mol%), catalyst (1 mol%) was placed in an

oil bath at 80°C after analysing at 0 h using ^{1}H NMR spectroscopy. Conversions and yields for each reaction were determined from the average of at least two runs by integration of ^{1}H NMR peaks relative to anisole. TON and TOF values were determined by using the conversion after 30 minutes.

X-ray Crystallography

A single crystal diffraction experiment of **C7** was performed using Quazar multi-layer optics monochromated Mo Kα radiation (k = 0.71069 Å) on a Bruker D8 Venture kappa geometry diffractometer with duo Iμs sources, a Photon 100 CMOS detector and APEX III control software.[62] Data reduction was performed using SAINT+,[62] and the intensities were corrected for absorption using SADABS.[62] Single crystals of **C1-C6**, **C8-C10**, were analysed on a Rigaku XtaLAB Synergy R diffractometer, with a rotating-anode X-ray source and a HyPix CCD detector. Data reduction and absorption were carried out using the CrysAlisPro (version 1.171.40.23a) software package.[63] All X-ray diffraction measurements were performed at 150.0(2) K, using an Oxford Cryogenics Cryostat. All structures were solved by direct methods with SHELXTS-2016[64] and refined using the SHELXL-2013[65] algorithm. All H atoms were placed in geometrically idealised positions and constrained to ride on their parent atoms. For data collection and refinement parameters, see the SI (Tables S1-S3). Deposition Number(s) 2244959 (**C1b**), 2244960 (**C3**), 2244961 (**C2a**), 2244962 (**C1c**), 2244963 (**C8**), 2244964 (**C9**), 2244965 (**C10**), 2244966 (**C7**), 2244967 (**C2b**), 2244968 (**C5**), 2244969 (**C4**), 2244970 (**C6**) contain the supplementary crystallographic data for this paper. These data are provided free of charge by the joint Cambridge Crystallographic Data Centre and Fachinformationszentrum Karlsruhe Access Structures service.

Electrochemistry

Cyclic voltammetry (CV) and linear sweep voltammetry (LSV) measurements were conducted on a BAS 100 B/W voltammograph. Measurements were made using 0.002 mol.dm^{-3} or saturated solutions of the complexes in dry acetonitrile containing 0.1 mol.dm^{-1} tetra-N-butylammonium hexafluorophosphate, $(NBu_4)(PF_6)$, as supporting electrolyte under a purified argon atmosphere at 25 °C. A three electrode cell, with a glassy carbon (surface area = 7.07 × 10^{-6} m^2) working electrode, a Pt auxiliary electrode, and a Ag wire as reference electrode, was used. Successive experiments under identical experimental conditions revealed all redox potentials were reproducible within 5 mV. In this work all cited potentials are referenced against the Fc/Fc+ couple as suggested by IUPAC. Ferrocene exhibited a formal reduction potential of $E^{0'}$ = 0.381 V vs. Ag/Ag$^+$, a peak separation of $\Delta E_p = E_{pa} - E_{pc}$ = 0.071 V, and i_{pa}/i_{pc} = 1.00, under the current experimental conditions. E_{pa} (E_{pc}) = anodic (cathodic) peak potential and i_{pa} (i_{pc}) = anodic (cathodic) peak current. The $E^{0'}$ of ferrocene (Fc/Fc$^+$) is reported to

be 0.644 V vs. SCE.[66] Linear sweep voltammogram (LSV) measurements were taken at a stationary electrode using a very slow scan rate of 2 mVs^{-1}.

Computational details

All calculations were carried out in the gas phase using DFT with the B3LYP hybrid functional as implemented in the gas phase using the Gaussian 16 program[67]. The basis set def2-tzvpp[68] in conjunction with Grimme's D3 empirical dispersion correction[69] was used for all atoms, where in addition the Stuttgart/Dresden (SDD) pseudopotential was used to describe the ruthenium electronic core. All geometries were optimised without any symmetry restrictions, ensuring that the local minima had zero imaginary vibrational frequencies. Orbital and spin density plots were generated using Chemcraft[70] using isovalues of 0.06 (MOs) and 0.03 (spin).

References

(1) Gonzalez-Baró, A. C.; Castellano, E. E.; Piro, O. E.; Parajón-Costa, B. S. Synthesis, crystal Structure and spectroscopic characterization of a novel bis (oxo-bridged) dinuclear vanadium(V)-dipicolinic acid complex. *Polyhedron* **2005**, *24*(1), 49–55. https://doi.org/10.1016/j.poly.2004.09.032.

(2) Pushpaveni, A.; Packiaraj, S.; Govindarajan, S.; McCandless, G. T.; Fronczek, C. F.; Fronczek, F. R. Structural resemblance and variation in transition metal complexes derived from dipicolinic acid and guanylhydrazine. *Inorg. Chim. Acta.* **2018**, *471*, 537–549. https://doi.org/10.1016/j.ica.2017.11.059.

(3) Mirzaei, M.; Eshtiagh-Hosseini, H.; Karrabi, Z.; Molčanov, K.; Eydizadeh, E.; Mague, J. T.; Bauzá, A.; Frontera, A. Crystal engineering with coordination compounds of Ni^{II}, Co^{II}, and Cr^{III} Bearing dipicolinic acid driven by the nature of the noncovalent interactions. *CrystEngComm* **2014**, *16*(24), 5352–5363. https://doi.org/10.1039/c4ce00325j.

(4) Garin, A. B.; Rakarić, D.; Andrić, E. K.; Kosanović, M. M.; Balić, T.; Perdih, F. Synthesis of monosubstituted dipicolinic acid hydrazide derivative and structural characterization of novel Co(III) and Cr(III) complexes. *Polyhedron* **2019**, *166*, 226–232. https://doi.org/10.1016/j.poly.2019.03.059.

(5) Abdolmaleki, S.; Ghadermazi, M.; Ashengroph, M.; Saffari, A.; Sabzkohi, S. M. Cobalt (II), zirconium(IV), calcium(II) complexes with dipicolinic acid and imidazole derivatives: X-Ray studies, thermal analyses, evaluation as *in vitro* antibacterial and cytotoxic agents. *Inorg. Chim. Acta.* **2018**, *480*, 70–82. https://doi.org/10.1016/j.ica.2018.04.047.

(6) Su, C.-C.; Chiu, S.-Y. Electronic and bonding properties of mixed-ligand pyridine-2,6-dicarboxylate copper(II) complexes: molecular structures of [Cu(4-dimethylaminopyridine)(pyridine-2,6-dicarboxylato)] and [Cu(*N*-methylimidazole)(pyridine-2,6-dicarboxylato)($0.5H_2O$)]. *Polyhedron* **1996**, *15*, 2623-2631. https://doi.org/10.1016/0277-5387(95)00542-0.

(7) Aliabadi, A.; Hakimi, M.; Hosseinabadi, F.; Motieiyan, E.; Rodrigues, V. H. N.; Ghadermazi, M.; Marabello, D.; Abdolmaleki, S. Investigation of X-Ray crystal structure and *in vitro* cytotoxicity of two Ga(III) Complexes containing pyridine dicarboxylic acid derivatives and 2-aminobenzimidazole. *J. Mol. Struct.* **2021**, *1223*, 129005. https://doi.org/10.1016/j.molstruc.2020.129005.

(8) Sharif, S.; Saeed, M.; Dege, N.; Bano, R.; Gilani, M. A.; Şahin, O.; Ahmad, S.; Ch, A. R. Solvothermal synthesis, crystal structure, thermal, magnetic properties and DFT computations of a Ytterbium(III) complex derived from pyridine-2,6-dicarboxylic acid. *J. Mol. Struct.* **2022**, *1260*, 132877. https://doi.org/10.1016/j.molstruc.2022.132877.

(9) Rud Moller, E.; Jorgensen, K. A. Chemistry of Molybdenaoxaziridines. A Study of Oxo(*N*-phenylhydroxylamido-O,*N*)(pyridine-2,6-dicarboxylato)(hexamethylphosphortriamide) molybdenum(VI) and its catalytic properties. *J. Am. Chem. Soc.* **1993**; 115, 11814-11822.

(10) Sukanya, D.; Prabhakaran, R.; Natarajan, K. Ruthenium(III) complexes of dipicolinic acid with PPh_3/$AsPh_3$ as co-ligand: Synthesis and structural characterization. *Polyhedron* **2006**, *25*(11), 2223–2228. https://doi.org/10.1016/j.poly.2006.01.023.

(11) Heydari, R.; Motieiyan, E.; Abdolmaleki, S.; Aliabadi, A.; Ghadermazi, M.; Bagheri, F.; Amiri Rudbari, H. Synthesis, X-Ray crystal structure, thermal behavior and evaluation as an *in vitro* cytotoxic agent of a tin(IV) complex containing dipicolinic acid. *J. Coord. Chem.* **2020**, *73*(16), 2347–2362. https://doi.org/10.1080/00958972.2020.1814955.

(12) Pitteri, B.; Cattalini, L.; Chessa, G.; Marangoni, G.; Stevanato, N.; Tobe, M. L. Nucleophilic Substitution Reactions at Planar Four-co-ordinate Monoanionic Platinum(II) Complexes. *J. Chem. Soc. Dalton Trans.* **1991**, 3049-3054.

(13) Espinet, P.; García-Orodea, E.; Miguel, J. A. Mesogenic Palladium Complexes with Pincer Ligands Derived from Dipicolinic Acid. *Inorg. Chem.* **2000**, *39*(16), 3645–3651. https://doi.org/10.1021/ic0001457.

(14) Aliabadi, A.; Motieiyan, E.; Hosseinabadi, F.; Ghadermazi, M.; Abdolmaleki, S. One-Pot synthesis, crystallographic characterization, evaluation as *in vitro* antibacterial and cytotoxic agents of two mercury(II) complexes containing pyridine dicarboxylic acid derivatives. *J. Mol. Struct.* **2021**, *1226*, 129405. https://doi.org/10.1016/j.molstruc.2020.129405.

(15) Wang, J.; De Kool, R. H. M.; Velders, A. H. Lanthanide-Dipicolinic Acid Coordination Driven Micelles with Enhanced Stability and Tunable Function. *Langmuir* **2015**, *31*(44), 12251–12259. https://doi.org/10.1021/acs.langmuir.5b03226.

(16) Abdolmaleki, S.; Aliabadi, A.; Ghadermazi, M. Two La(III) complexes containing pyridine-2,6-dicarboxylate as *in vitro* potent cytotoxic agents toward human lymphocyte cells. *Inorg. Chim. Acta.* **2022**, *542*, 121152. https://doi.org/10.1016/j.ica.2022.121152.

(17) Zohrevandi, M.; Abdolmaleki, S.; Ghadermazi, M.; Gholiee, Y.; Aliabadi, A.; Motieiyan, E.; Hakimi, M.; Marabello, D. Synthesis, characterization, crystallographic structure, theoretical studies, and *in vitro* cytotoxicity assessment of two Gd(III) and Ce(IV) complexes containing pyridine-2,6-dicarboxylate. *Polyhedron* **2022**, *211*, 115561. https://doi.org/10.1016/j.poly.2021.115561.

(18) Heydari, R.; Motieiyan, E.; Aliabadi, A.; Abdolmaleki, S.; Ghadermazi, M.; Yarmohammadi, N. Synthesis, crystallographic studies, electrochemical and *in vitro* cytotoxicity properties of two Mn(II) and U(IV) complexes containing dipicolinic acid and 4-dimethylaminopyridine. *Polyhedron* **2020**, *181*, 114477. https://doi.org/10.1016/j.poly.2020.114477.

(19) Agarwal, R.; Dumpala, R. M. R.; Sharma, M. K.; Yadav, A. K.; Ghosh, T. K. Stabilization of uranyl(v) by dipicolinic acid in aqueous medium. *Dalton Trans.* **2021**, *50*(4), 1486–1495. https://doi.org/10.1039/d0dt03961f.

(20) Uçar, I.; Bulut, I.; Bulut, A.; Karadağ, A. Polymeric and monomeric dipicolinate complexes with 4-hydroxymethyl pyridine: spectral, structural, thermal and electrochemical characterization. *Struct. Chem.* **2009**, *20*(5), 825–838. https://doi.org/10.1007/s11224-009-9475-3.

(21) Maser, L.; Vondung, L.; Langer, R. The ABC in pincer chemistry – From amine- to borylene- and carbon-based pincer-ligands. *Polyhedron* **2018**, *143*, 28–42. https://doi.org/10.1016/j.poly.2017.09.009.

(22) Lawrence, M. A. W.; Green, K. A.; Nelson, P. N.; Lorraine, S. C. Review: Pincer Ligands—Tunable, versatile and applicable. *Polyhedron*. **2018**, *143*, 11–27. https://doi.org/10.1016/j.poly.2017.08.017.

(23) Alig, L.; Fritz, M.; Schneider, S. First-Row Transition Metal (De)Hydrogenation Catalysis Based on Functional Pincer Ligands. *Chem. Rev*. **2019**, 119(4), 2681–2751. https://doi.org/10.1021/acs.chemrev.8b00555.

(24) Choi, J.; MacArthur, A. H. R.; Brookhart, M.; Goldman, A. S. Dehydrogenation and Related Reactions Catalyzed by Iridium Pincer Complexes. *Chem. Rev*. **2011**, 111(3), 1761–1779. https://doi.org/10.1021/cr1003503.

(25) González-Sebastián, L.; Morales-Morales, D. Cross-coupling reactions catalysed by palladium pincer complexes. A review of recent advances. *J. Organomet. Chem.* **2019**, *893*, 39–51. https://doi.org/10.1016/j.jorganchem.2019.04.021.

(26) Peris, E.; Crabtree, R. H. Key Factors in Pincer Ligand Design. *Chem. Soc. Rev.* **2018**, *47* (6), 1959–1968. https://doi.org/10.1039/c7cs00693d.

(27) Polukeev, A. V.; Petrovskii, P. V.; Peregudov, A. S.; Ezernitskaya, M. G.; Koridze, A. A. Dehydrogenation of Alcohols by Bis(phosphinite) Benzene Based and Bis(phosphine) Ruthenocene Based Iridium Pincer Complexes. *Organometallics* **2013**, *32*(4), 1000–1015. https://doi.org/10.1021/om300921q.

(28) Gupta, M.; Hagen, C.; Kaska, W. C.; Cramer, R. E.; Jensen, C. M. Catalytic Dehydrogenation of Cycloalkanes to Arenes by a Dihydrido Iridium P-C-P Pincer Complex. *J. Am. Chem. Soc.* **1997**, *119*(4), 840-841. https://doi.org/10.1021/ja962560x

(29) Wang, Y.; Huang, Z.; Liu, G.; Huang, Z. A New Paradigm in Pincer Iridium Chemistry: PCN Complexes for (De)Hydrogenation Catalysis and Beyond. *Acc. Chem. Res.* **2022**, *55*(15), 2148–2161. https://doi.org/10.1021/acs.accounts.2c00311.

(30) Gordon, B. M.; Lease, N.; Emge, T. J.; Hasanayn, F.; Goldman, A. S. Reactivity of Iridium Complexes of a Triphosphorus-Pincer Ligand Based on a Secondary Phosphine. Catalytic Alkane Dehydrogenation and the Origin of Extremely High Activity. *J. Am. Chem. Soc.* **2022**, *144*(9), 4133–4146. https://doi.org/10.1021/jacs.1c13309.

(31) Tran, R.; Canote, C. A.; Kilyanek, S. M. Mechanistic Studies of the Deoxydehydration of Polyols Catalyzed by a Mo(VI) Dioxo(pyridine-2,6-dicarboxylato) Complex. *Organometallics* **2023**, *42*(11), 1190-1197. https://doi.org/10.1021/acs.organomet.3c00001.

(32) Drzeżdżon, J.; Pawlak, M.; Gawdzik, B.; Wypych, A.; Kramkowski, K.; Kowalczyk, P.; Jacewicz, D. Dipicolinate Complexes of Oxovanadium(IV) and Dioxovanadium(V) with 2-Phenylpyridine and 4,4′-Dimethoxy-2,2′-Bipyridyl as New Precatalysts for Olefin Oligomerization. *Materials* **2022**, *15*(4), 1379. https://doi.org/10.3390/ma15041379.

(33) Gürbüz, N.; Yaşar, S.; Özcan, E. Ö.; Özdemir, I.; Çetinkaya, B. Transfer Hydrogenation of Ketones by Ruthenium Complexes Bearing Benzimidazol-2-ylidene Ligands. *Eur. J. Inorg. Chem.* **2010**, *2010*(19), 3051–3056. https://doi.org/10.1002/ejic.201000181.

(34) Wang, R.; Qin, L.; Wang, X.; Chen, B.; Zhao, Y.; Gao, G. Polymer supported N-Heterocyclic carbene ruthenium complex catalyzed transfer hydrogenation of ketones. *Catal. Commun.* **2020**, *138*, 105924. https://doi.org/10.1016/j.catcom.2019.105924.

(35) Ma, X.; Guillet, S. G.; Liu, Y.; Cazin, C. S. J.; Nolan, S. P. Simple synthesis of [Ru(CO_3)(NHC)(*p*-cymene)] complexes and their use in transfer hydrogenation catalysis. *Dalton Trans.* **2021**, *50*(37), 13012–13019. https://doi.org/10.1039/d1dt02098f.

(36) Amason, E. K.; Rajabimoghadam, K.; Baughman, N. N.; Ghareeb, C. R.; Bourgeois, S. K.; Keuk, C.; Manacsa, G.; Popp, B. V.; Garcia-Bosch, I.; Ferrence, G. M.; Joslin, E. E. Synthesis and Reactivity of Ampy-Based Ruthenium(II) Catalysts for Transfer Hydrogenation of Ketones. *Organometallics* **2022**, *41*(6), 686–697. https://doi.org/10.1021/acs.organomet.1c00444.

(37) Hoque, M. A.; Gil-Sepulcre, M.; Benet-Buchholz, J.; Llobet, A.; Gimbert-Suriñach, C. Synthesis, Electrochemical Characterization, and Water Oxidation Chemistry of Ru Complexes Containing the 2,6-Pyridinedicarboxylato Ligand. *Inorg. Chem.* **2020**, *59*(16), 11432–11441. https://doi.org/10.1021/acs.inorgchem.0c01215.

(38) Khan, S.; Naskar, S. Chemical and electrochemical water oxidation catalyzed by heteroleptic Ru(III) complexes of anionic 2,6 pyridine dicarboxylate ligand: Experimental and theoretical study. *Polyhedron* **2022**, *222*, 115898. https://doi.org/10.1016/j.poly.2022.115898.

(39) Daniel, Q.; Duan, L.; Timmer, B. J. J.; Chen, H.; Luo, X.; Ambre, R.; Wang, Y.; Zhang, B.; Zhang, P.; Wang, L.; Li, F.; Sun, J.; Ahlquist, M.; Sun, L. Water Oxidation Initiated by In Situ Dimerization of the Molecular Ru(pdc) Catalyst. *ACS Catal.* **2018**, *8*(5), 4375–4382. https://doi.org/10.1021/acscatal.7b03768.

(40) Hoque, M. A.; Benet-Buchholz, J.; Llobet, A.; Gimbert-Suriñach, C. Catalytic Oxidation of Water to Dioxygen by Mononuclear Ru Complexes Bearing a 2,6-Pyridinedicarboxylato Ligand. *ChemSusChem* **2019**, *12*(9), 1949–1957. https://doi.org/10.1002/cssc.201802996.

(41) Yang, Y.; Yang, J.; Li, F.; Liao, R.; Duan, L. Water Oxidation Catalyzed by Ruthenium Complexes with 4-Hydroxypyridine-2,6-Dicarboxylate as a Negatively Charged Tridentate Ligand. *Eur. J. Inorg. Chem.* **2020**, *2020*(23), 2238–2245. https://doi.org/10.1002/ejic.202000184.

(42) Rabten, W.; Kärkäs, M. D.; Åkermark, T.; Chen, H.; Liao, R-Z.; Tinnis, F.; Sun, J.; Siegbahn, P. E. M.; Andersson, P. G.; Åkermark, B. Catalytic Water Oxidation by a Molecular Ruthenium Complex: Unexpected Generation of a Single-Site Water Oxidation Catalyst. *Inorg. Chem.* **2015**, *54*(10), 4611–4620. https://doi.org/10.1021/ic502755c.

(43) Tong, L.; Wang, Y.; Duan, L.; Xu, Y.; Cheng, X.; Fischer, A.; Ahlquist, M. S. G.; Sun, L. Water Oxidation Catalysis: Influence of Anionic Ligands upon the Redox Properties and Catalytic Performance of Mononuclear Ruthenium Complexes. *Inorg. Chem.* **2012**, *51*(6), 3388–3398. https://doi.org/10.1021/ic201348u.

(44) Shatskiy, A.; Lomoth, R.; Abdel-Magied, A. F.; Rabten, W.; Laine, T. M.; Chen, H.; Sun, J.; Andersson, P. G.; Kärkäs, M. D.; Johnston, E. V.; Åkermark, B. Catalyst-solvent interactions in a dinuclear Ru-based water oxidation catalyst. *Dalton Trans.* **2016**, *45*(47), 19024–19033. https://doi.org/10.1039/c6dt03789e.

(45) Zhang, Y.; Zhao, L.; Zhang, H.; Huang, R.; Zhao, J. Oxidation of alkanes and secondary alcohols to ketones with *tert*-butyl hydroperoxide catalyzed by a water-soluble ruthenium complex under solvent-free conditions. *Appl. Organomet. Chem.* **2017**, *31*(9), e3709. https://doi.org/10.1002/aoc.3709.

(46) Zhang, Y.; Liu, L.; Cao, X.; Zhao, J. Synthesis, single crystal structure and efficient catalysis for alcohol oxidation of a novel Ru(II) complex with both a N,N,N-tridentate ligand and a pyridinedicarboxylate. *Polyhedron* **2016**, *105*, 170–177. https://doi.org/10.1016/j.poly.2015.08.047.

(47) Wang, J. X.; Zhou, X. T.; Han, Q.; Guo, X-X.; Liu, X-H.; Xue, C.; Ji, H. B. Efficient and selective oxidation of alcohols to carbonyl compounds at room temperature by a ruthenium complex catalyst and hydrogen peroxide. *New J. Chem.* **2019**, *43*(48), 19415–19421. https://doi.org/10.1039/c9nj04393d.

(48) Xie, Y. F.; Jia, A. Q.; Zhu, H.; Shi, H-T.; Zhang, Q-F. Synthesis and reactivity of ruthenium(II) complexes with 1,5-cyclooctadiene and pyridine-2,6-dicarboxylato ligands. *Inorg. Chim. Acta.* **2015**, *438*, 31–36. https://doi.org/10.1016/j.ica.2015.08.028.

(49) Nangia, A. K.; Desiraju, G. R. Crystal Engineering: An Outlook for the Future. *Angew. Chem. Int. Ed.* **2019**, *58*(13), 4100–4107. https://doi.org/10.1002/anie.201811313.

(50) van Vuuren, E.; Malan, F. P.; Landman, M. Cyclometallated iridium NHC complexes containing self-isomerised ligands as catalysts for hydrosilylation and transfer hydrogenation reactions. *New J. Chem.* **2023**, *47*(11), 5203–5215. https://doi.org/10.1039/d2nj05727a.

(51) Balat, M. Global Trends on the Processing of Bio-Fuels. *Int. J. Green Energy* **2008**, *5*(3), 212–238. https://doi.org/10.1080/15435070802107322.

(52) Swart, M. R.; Marais, C.; Erasmus, E. Comparison of the Spectroscopically Measured Catalyst Transformation and Electrochemical Properties of Grubbs' First- And Second-Generation Catalysts. *ACS Omega* 2021, *6*(43), 28642–28653. https://doi.org/10.1021/acsomega.1c03109.

(53) Atkins, P.; Overton, T.; Rourke, J.; Weller, M.; Armstrong, F. (2010). *Shriver and Atkins' Inorganic Chemistry* (5th ed.). Oxford: Oxford University Press.

(54) Fourie, E.; Janse van Rensburg, J. M.; Swarts, J. C. Synthesis, crystal structure and comparative electrochemistry of metallocenyldiphenylphosphines of ruthenocene, osmocene, ferrocene and cobaltocenium hexafluorophosphate. *J. Organomet. Chem.* 2014, 754, 80-87.

(55) Swarts, P. J.; Erasmus, E.; Fourie, E. Comparison of synthetic, spectroscopic, computational and electrochemical aspects of ferrocenyl-containing β-diketones, β-ketoesters and β-ketoamides. *Polyhedron* **2021**, *205*, 115279. https://doi.org/10.1016/j.poly.2021.115279.

(56) Malan, F. P.; Singleton, E.; Van Rooyen, P. H.; Landman, M. Tandem transfer hydrogenation-epoxidation of ketone substrates catalysed by alkene-tethered Ru(II)-NHC Complexes. *New J. Chem.* **2019**, *43*(22), 8472–8481. https://doi.org/10.1039/c9nj01220f.

(57) Malan, F. P. Structural, Electrochemical and Catalytic Elucidation of Cyclooctadiene Ru(II)-Nitrile Complexes of the Type $[RuCl_2(cod)(NCR)_2]$. *ChemistrySelect* **2022**, *7*(18), e202201432. https://doi.org/10.1002/slct.202201432.

(58) Conradie, J. Tris(β-ketoiminato)ruthenium(III) – Structural and electronic data of the neutral, oxidized and reduced forms. *Data in Brief* **2020**, *28*, 104833. https://doi.org/10.1016/j.dib.2019.104833.

(59) van der Westhuizen, D.; von Eschwege, K. G.; Conradie, J. Electrochemistry and spectroscopy of substituted $[Ru(phen)_3]^{2+}$ and $[Ru(bpy)_3]^{2+}$ complexes. *Electrochim. Acta.* **2019**, *320*, 134540. https://doi.org/10.1016/j.electacta.2019.07.051.

(60) Pearson, R. G. The Principle of Maximum Hardness. *Acc. Chem. Res.* **1993**, 26(5), 250-255. https://doi.org/10.1021/ar00029a004

(61) R.J. Errington. *Advanced Practical Inorganic and Metalorganic Chemistry, Blackie Academic & Professional, London*; **1997**.

(62) APEX3 (including SAINT and SADABS), Bruker AXS Inc., Madison, WI, (2016).

(63) Rigaku Oxford Diffraction, CrysAlisPro Software system, (2018).

(64) Sheldrick, G. M., SHELXT–Integrated Space-Group and Crystal-Structure Determination. Acta Crystallogr. A **2015**, *71*(1), 3-8.

(65) Sheldrick, G. M., Crystal Structure Refinement with SHELXL. Acta Crystallogr. C **2015**, *71*(1), 3-8.

(66) Magdzinski, E.; Gobbo, P.; Martin, C. D.; Workentin, M. S.; Ragogna, P. J. The Syntheses and Electrochemical Studies of a Ferrocene Substituted Diiminopyridine Ligand and Its P, S, Se, and Te Complexes. *Inorg. Chem.* **2012**, 51(15), 8425-8432. https://doi.org/10.1021/ic300974u.

(67) Gaussian 16, Revision C.01, Frisch, M. J.; Trucks, G. W.; Schlegel, H. B.; Scuseria, G. E.; Robb, M. A.; Cheeseman, J. R.; Scalmani, G.; Barone, V.; Petersson, G. A.; Nakatsuji, H.; Li, X.; Caricato, M.; Marenich, A. V.; Bloino, J.; Janesko, B. G.; Gomperts, R.; Mennucci, B.; Hratchian, H. P.; Ortiz, J. V.; Izmaylov, A. F.; Sonnenberg, J. L.; Williams-Young, D.; Ding, F.; Lipparini, F.; Egidi, F.; Goings, J.; Peng, B.; Petrone, A.; Henderson, T.; Ranasinghe, D.; Zakrzewski, V. G.; Gao, J.; Rega, N.; Zheng, G.; Liang, W.; Hada, M.; Ehara, M.; Toyota, K.; Fukuda, R.; Hasegawa, J.; Ishida, M.; Nakajima, T.; Honda, Y.; Kitao, O.; Nakai, H.; Vreven, T.; Throssell, K.; Montgomery, J. A., Jr.; Peralta, J. E.; Ogliaro, F.; Bearpark, M. J.; Heyd, J. J.; Brothers, E. N.; Kudin, K. N.; Staroverov, V. N.; Keith, T. A.; Kobayashi, R.; Normand, J.; Raghavachari, K.; Rendell, A. P.; Burant, J. C.; Iyengar, S. S.; Tomasi, J.; Cossi, M.; Millam, J. M.; Klene, M.; Adamo, C.; Cammi, R.; Ochterski, J. W.; Martin, R. L.; Morokuma, K.; Farkas, O.; Foresman, J. B.; Fox, D. J. Gaussian, Inc., Wallingford CT, 2016.

(68) Weigend, F.; Ahlrichs, R. Balanced basis sets of split valence, triple zeta valence and quadruple zeta valence quality for H to Rn: Design and assessment of accuracy. *Phys. Chem. Chem. Phys.* **2005**, 7(18), 3297-3305. https://doi.org/10.1039/B508541A

(69) Grimme, S., Semiempirical GGA-Type Density Functional Constructed with a Long range Dispersion Correction. *J. Comput. Chem.* **2006**, 27, 1787-1799.

(70) Chemcraft – Graphical Software for Visualization of Quantum Chemistry Computations. https://www.chemcraftprog.com.